Vibrationally resolved above-threshold ionization in NO molecules by intense ultrafast two-color laser pulses: An experimental and theoretical study

Yong Liu,[1] Wenhui Hu,[2] Sizuo Luo,[2,3,*] Kai-Jun Yuan,[2,4,†] Zhigang Sun,[1,5] André D. Bandrauk,[4] and Dajun Ding[2,3,‡]

[1]*State Key Laboratory of Molecular Reaction Dynamics, Dalian Institute of Chemical Physics, Chinese Academy of Sciences, Dalian 116023, China*

[2]*Institute of Atomic and Molecular Physics, Jilin University, Changchun 130012, China*

[3]*Jilin Provincial Key Laboratory of Applied Atomic and Molecular Spectroscopy, Jilin University, Changchun 130012, China*

[4]*Laboratoire de Chimie Théorique, Faculté des Sciences, Université de Sherbrooke, Sherbrooke, Québec, Canada J1K 2R1*

[5]*Center for Advanced Chemical Physics and 2011 Frontier Centre for Quantum Science and Technology, University of Science and Technology of China, 96 Jinzhai Road, Hefei 230026, China*

(Received 16 May 2019; published 5 August 2019)

We present above-threshold ionization (ATI) in the molecule nitric oxide, NO, by intense (10^{12}–10^{13} W/cm^2) two-color femtosecond laser pulses. Vibrationally resolved coherent interference phenomena of multiphoton and multipathway ionization processes have been investigated by measuring experimentally and modeling theoretically the molecular photoionization yields. We find that the ATI photoelectron distribution of NO, initiated from degenerate electronic and vibrational states, depends on the relative phase of the two pulses, the kinetic energy, and emission angle of the photoelectrons. This dependence codes the information of interference effects of molecular electronic states. AC Stark effects modulate interference patterns in ATI spectra. Moreover, the ATI spectra exhibit peak energy dependencies that illustrate interference effects from coherent couplings between various ionization channels. These features reflect the molecular property and the multiple channel ionization interference effects in ATI processes. The results allow to explore coherent electron-vibration processes in ultrafast molecular photoionization.

DOI: 10.1103/PhysRevA.100.023404

I. INTRODUCTION

The interactions of intense femtosecond (1 fs = 10^{-15} s) laser pulses with atoms, molecules, and surfaces have been attracting considerable attention and become important issues in the fields of photophysics and photochemistry [1–3]. In past decades, numerous interesting phenomena have been reported, including bond softening and bond hardening [4–8], above-threshold dissociation [8–10], high-order harmonic generation (HHG) [11,12], quantum coherence in single molecules [13,14], light-induced conical intersection [15–17], coherent control of molecular reactions [18,19], etc. Above-threshold ionization (ATI) as a fundamental strong field phenomenon has been widely studied in both experiments and theories, e.g., [20–24]. By measuring ATI spectra one can image atomic and molecular orbitals using recolliding electrons by laser-induced electron diffraction [25–27] and by photoelectron holography [28,29]. Photoelectron destructive interference in angular high-order ATI spectra of diatomic molecules O_2 and N_2 involving four geometric orbits has been found experimentally and has been well confirmed theoretically based on molecular strong field approximation simulations [30]. As a consequence of electron interference between the forward-scattered and nonscattered electron trajectories, multiple holographic patterns are observed in ATI momentum distributions [31], thus providing a tool to image molecular structure.

Nitric oxide, NO, is an very important molecule in human physiology and has many applications in medicine. Many efforts have been devoted to investigating its physical and chemical molecular characteristics in the past. Femtosecond multiphoton ionization spectroscopy has been used as an efficient tool to study ultrafast molecular dynamics of NO, e.g., [32–46]. The nonadiabatic coupling between the $B\,^2\Pi$ and $C\,^2\Pi$ states of NO has been studied by multiphoton photoelectron spectroscopy (PES) with a weak continuous wave (cw) laser field [34]. Femtosecond time-resolved photoelectron spectroscopy (TRPES) has also been used to study $2+1$ multiphoton ionization processes of NO via the $A\,^2\Sigma^+$ (γ-band), $B\,^2\Pi$ (β-band), and $C\,^2\Pi$ (δ-band) states [37]. The dependence of the coupling between $B\,^2\Pi$ and $C\,^2\Pi$ states on the laser intensity by simulations of the femtosecond TRPES of the molecule NO has been studied [41]. Moreover, the field modulation of populations of NO Rydberg states has been studied by femtosecond time-resolved photoelectron imaging [42]. It has been found that the Rydberg-valence coupling between the $A\,^2\Sigma^+$ Rydberg state and the $B\,^2\Pi$ valence state plays a key role in forming photoelectrons with kinetic energy of 0.37 eV by a strong pump laser field. Dynamic Stark effects of Rydberg states of NO have also been studied by experimental fluorescence spectra and theoretical calculations [43–45]. These studies provide the important molecular spectroscopic parameters, allowing to control the reactions of the molecule NO by intense laser pulses.

*luosz@jlu.edu.cn
†kaijun.yuan@usherbrooke.ca
‡dajund@jlu.edu.cn

Quantum coherent interference of electronic states is an important issue in reactions of molecules [47–59], which offers a new way to manipulate the nuclear and electronic dynamics. In a coherent resonant excitation process, the interference of electronic states can be used to control molecular HHG [47,48]. As a result, measurements of HHG spectra offer a tool to monitor the resulting attosecond (1 as $= 10^{-18}$ s) electron dynamics in molecules [60]. By using the high sensitivity of angularly resolved electron spectroscopy, electronic state interference in the CH_3Cl molecule was investigated [50]. By preparing a superposition state in benzene with a laser pulse, coherent interference effects between ground and excited electronic states lead to angular electronic fluxes [55], which is shown to be sensitive to the polarization and helicity of the laser pulse, and the symmetry property of the excited electronic state [56]. Interference effects of molecular multiple orbitals on HHG are also demonstrated experimentally and theoretically [57,58]. Zero-width resonances that result from destructive interference between two outgoing wave components originating from vibrational states have also been proposed in H_2^+ [59]. It still remains a difficulty to characterize the property of the energetically degenerate electronic-vibrational state interference in ultrafast molecular dynamics. We have shown that with two-color femtosecond laser pulses, angular-resolved photoelectron spectra show dependence on the pulse phase and the emission angle, illustrating the interference effect of electronic states [51]. Vibrationally resolved photoionization in molecules has been presented [52,53], which can be used to reconstruct the associated autoionization dynamics with subfemtosecond time resolution [54]. However, the interference effects of electronic states on vibrationally resolved photoionization, to the best of our knowledge, have not been studied. In this work, we focus on vibrationally resolved molecular ATI spectra in NO by intense phase-controlled two-color femtosecond laser pulses. We measure *experimentally* and model *theoretically* molecular photoionization yields to explore vibronic coherent interference processes. The interference between degenerate vibrational levels in different electronic states determines the phase and energy dependence of the photoelectron angular distributions in ATI, thus opening a route to gain insights into the vibrational electron processes in molecules by intense ultrafast laser pulses.

The paper is arranged as follows: In Sec. II, we briefly describe the experimental setup and numerical simulation methods. Our experimental measurements, numerical simulations, and theoretical models are presented in Sec. III. Interference patterns in ATI spectra illustrate the coherent molecular vibronic processes in intense phase-controlled two-color laser fields. The theoretical analysis describes the experimental observations. Finally, we summarize our findings in Sec. IV.

II. EXPERIMENTAL AND THEORETICAL METHODS

A. Experimental design

Our experiments use a velocity map imaging spectrometer (VMIs) [61] to detect the ultrafast phase-controlled photoelectron spectra produced from the two-color lasers interacting with a supersonic NO(1% NO seeded in neon). The

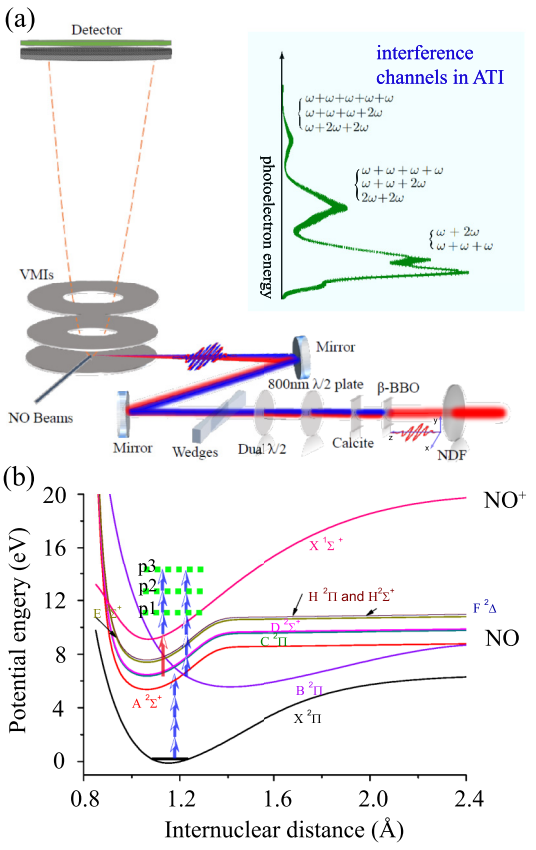

FIG. 1. (a) Schematic illustration of the experimental setup for producing and measuring photoelectron momentum spectra by intense two-color phase-controlled laser pulses. Insets display interference channels of photoelectrons in ATI. (b) Molecular potential energy curves of NO adopted from Ref. [65] and two-color excitation and ionization processes. Arrows indicate the possible multiphoton excitation and ionization pathways by (blue) 800-nm ($\hbar\omega = 1.55$ eV) and (red) 400-nm ($2\hbar\omega = 3.1$ eV) pulses. Symbols p1, p2, and p3 denote the three lowest-order ATI peaks in photoelectron spectra.

schematic illustration of the experimental setup is presented in Fig. 1(a) and the detail is briefly described in the following. The laser beam with 800-nm wavelength (ω), 50-fs duration, 4-mJ per pulse energy, and 1-kHz repetition rate from a chirped pulse amplified (CPA) Ti:sapphire laser system is introduced into a β-BBO crystal to obtain its double-frequency 400-nm (2ω) pulse. Then, the $\omega + 2\omega$ beam passes through a calcite crystal (4.5 mm) to compensate the time delay caused by the group velocity delay of 800-nm and 400-nm laser beams in the whole optical path. A 800-nm $\lambda/2$ plate and a dual $\lambda/2$ plate are used to rotate the polarization of the two lasers into the same direction parallel with the detector plane, and the relative phase between the two color lasers is controlled by accurately moving the fused silica wedges. After that, this phase-controlled laser beam is focused into the VMIs by a concave mirror ($f = 30$ cm) and interacts with the molecular beam. The generated electrons are guided onto a MCP-phosphor screen assembly by inhomogeneous electric fields between three electrodes in the VMIs. The images of the electron distribution are recorded with a CCD camera and transfer to a computer for further data processing. We have

recorded the images of electron momentum distribution at different relative phases between 800- and 400-nm lasers with a step of 0.08π, and the iterative Abel inversion method [62] has been used to reconstruct the three-dimensional (3D) slice and extract the energy spectra and angular distributions.

The two-color collinear laser field is represented as

$$E(t) = E_\omega f(t)\cos(\omega t) + E_{2\omega} f(t)\cos(2\omega t + \Delta\phi), \quad (1)$$

where $E_{\omega/2\omega}$ is the amplitude of the electric field, corresponding to the pulse intensity $I_{\omega/2\omega} = c\epsilon_0 E^2_{\omega/2\omega}/2$, where c is the speed of light and ϵ_0 denotes the permittivity of free space, and $f(t)$ denotes the common pulse envelope. The laser pulse propagates along the z axis with its field vector polarized along the x axis, as illustrated in Fig. 1(a). Frequencies ω and 2ω correspond to wavelengths 800 and 400 nm, and $\Delta\phi$ is the relative phase of the two laser pulses. The ω pulse intensity is adjusted by rotating the NDF (neutral density filter) before the β-BBO crystal, and the intensity of the 2ω pulse is controlled by rotating the phase-matching angle of the β-BBO crystal, and the intensity ratio $I_{2\omega}/I_\omega$ of the two-color laser field is controlled to 0.08 in our experiments, i.e., the pulse intensities $I_\omega = 2.2 \times 10^{13}$ W/cm^2 and $I_{2\omega} = 1.8 \times 10^{12}$ W/cm^2. The intensities of the two-color laser are separately calibrated by measuring the intensity-dependent AC Stark shift of the ATI peaks of Xe, as mentioned previously [63,64]. The pulse FWHMs are approximately $T_\omega = 50$ fs and $T_{2\omega} = 60$ fs. Based on our experiences and the comparison with the previous results, we estimated the uncertainty of 800 nm is less than 10% and that of 400 nm is less than 30%, due to the exact calibration of laser intensities during experiments still is a challenging task.

B. Theoretical simulation methods

The potential energy curves of the NO molecule and its ion NO^+ are obtained from Ref. [65], as shown in Fig. 1(b). The NO molecule is initially in the ground state $X\,^2\Pi$, from which a two-color laser pulse at wavelengths 400 and 800 nm excites and ionizes the molecule. The ionization continuum $X\,^1\Sigma^+$ state of the NO^+ ion is numerically discretized into a band of quasicontinuum levels in terms of the electronic eigenstates $|E_n\rangle$, $n = 0, 1, 2, \ldots, N$, containing the core and free electron [66,67]. These states are labeled according to the kinetic energy of the ejected electron, where E_0 and E_N are the smallest and largest energies which can be transferred to the electron, respectively. The ionic states are labeled according to the kinetic energy of the ejected electron [66,67]

$$\psi_I(R,\theta,t) = \sum_{n=1}^{N} \chi_{In}(R,\theta,t)|E_n\rangle, \quad (2)$$

where χ_{In} are the nuclear wave functions of NO^+, with the emission of an electron with kinetic energy $E_n = E_0 + n(E_N - E_0)/N$, $n = 0, 1, 2, \ldots, N$, where a maximum $N = 200$ is used to discretize the quasicontinuum state of NO^+. In the Born-Oppenheimer approximation, the nuclear wave function $\chi(R,\theta,t)$ of each electronic state is obtained by solving the appropriate time-dependent Schrödinger equation (TDSE)

$$i\hbar\frac{\partial}{\partial t}\chi(R,\theta,t) = \hat{\mathbf{H}}\chi(R,\theta,t). \quad (3)$$

The Hamiltonian of the molecular system interacting with the electric field of the laser pulse can be written as

$$\hat{\mathbf{H}} = -\frac{\hbar^2}{2m}\frac{\partial^2}{\partial R^2}\hat{\mathbf{I}} + \frac{\hat{\mathbf{J}}^2}{2mR^2} + \hat{\mathbf{V}}(R) + \hat{\mathbf{V}}_L(R,\theta,t), \quad (4)$$

where m is the reduced mass of the NO molecule, R is internuclear distance, $\hat{\mathbf{I}}$ the unitary matrix, $\hat{\mathbf{J}}^2$ the rotational angular momentum operator, and θ the angle between the directions of the electric field and the molecular axis. The potential energy matrix $\hat{\mathbf{V}}(R)$ is given as

$$\hat{\mathbf{V}}(R) = \mathrm{diag}(V_X, V_A, V_B, V_C, V_D, V_E, V_F, V_H, V_{H'}, V_{I0}, \ldots, V_{IN}) \quad (5)$$

where $V_X, V_A, \ldots, V_{H'}$ are the corresponding potential energies of the electronic states of the NO molecule, as shown in Fig. 1(b). $V_{In}(R) = V_I(R) + E_n$ is the discretized potential, and V_I is the potential energy of the $X\,^1\Sigma^+$ states of the ion NO^+. The coupling term of the molecule NO and its cation NO^+ interacting with the two-color laser pulse can be written as

$$\hat{\mathbf{V}}_L(R,\theta,t) = \begin{pmatrix}
0 & V_{XA} & V_{XB} & 0 & 0 & 0 & 0 & 0 & 0 & V_{XI0} & \cdots & V_{XIn} & \cdots & V_{XIN} \\
V_{XA} & 0 & 0 & V_{AC} & V_{AD} & 0 & 0 & 0 & 0 & V_{AI0} & \cdots & V_{AIn} & \cdots & V_{AIN} \\
V_{XB} & 0 & 0 & 0 & V_{BD} & 0 & 0 & 0 & 0 & V_{BI0} & \cdots & V_{BIn} & \cdots & V_{BIN} \\
0 & V_{AC} & 0 & 0 & 0 & V_{CE} & V_{CF} & V_{CH} & V_{CH'} & V_{CI0} & \cdots & V_{CIn} & \cdots & V_{CIN} \\
0 & V_{AD} & V_{BD} & 0 & 0 & V_{DE} & 0 & V_{DH} & V_{DH'} & V_{DI0} & \cdots & V_{DIn} & \cdots & V_{DIN} \\
0 & 0 & 0 & V_{CE} & V_{DE} & 0 & 0 & 0 & 0 & V_{EI0} & \cdots & V_{EIn} & \cdots & V_{EIN} \\
0 & 0 & 0 & V_{CF} & 0 & 0 & 0 & 0 & 0 & V_{FI0} & \cdots & V_{FIn} & \cdots & V_{FIN} \\
0 & 0 & 0 & V_{CH} & V_{DH} & 0 & 0 & 0 & 0 & V_{HI0} & \cdots & V_{HIn} & \cdots & V_{HIN} \\
0 & 0 & 0 & V_{CH'} & V_{DH'} & 0 & 0 & 0 & 0 & V_{H'I0} & \cdots & V_{H'In} & \cdots & V_{H'IN} \\
V_{XI0} & V_{AI0} & V_{BI0} & V_{CI0} & V_{DI0} & V_{EI0} & V_{FI0} & V_{HI0} & V_{H'I0} & 0 & \cdots & 0 & \cdots & 0 \\
\vdots & \vdots & \vdots & \vdots & \vdots & \vdots & \vdots & \vdots & \vdots & \vdots & \ddots & \vdots & \ddots & \vdots \\
V_{XIn} & V_{AIn} & V_{BIn} & V_{CIn} & V_{DIn} & V_{EIn} & V_{FIn} & V_{HIn} & V_{H'In} & 0 & \cdots & 0 & \cdots & 0 \\
\vdots & \vdots & \vdots & \vdots & \vdots & \vdots & \vdots & \vdots & \vdots & \vdots & \ddots & \vdots & \ddots & \vdots \\
V_{XIN} & V_{AIN} & V_{BIN} & V_{CIN} & V_{DIN} & V_{EIN} & V_{FIN} & V_{HIN} & V_{H'IN} & 0 & \cdots & 0 & \cdots & 0
\end{pmatrix} \quad (6)$$

with

$$V_{ij} = \begin{cases} -\mu_{ij}(R)E(t)\cos\theta & \text{if } \Delta\Lambda = 0, \\ -\mu_{ij}(R)E(t)\sin\theta & \text{if } \Delta\Lambda = \pm 1, \end{cases} \tag{7}$$

and

$$V_{iIn} = -\mu_{iI}(R)E(t)\cos\theta, \tag{8}$$

where $i, j = X$, A, B, C, D, E, F, H, and H' denote the electronic states of the molecule NO in Fig. 1(b), and $n = 0, 1, \ldots, N$, presents the discretized quasicontinuum level of the cation NO^+. $\Delta\Lambda = 0$ and ± 1 denote parallel transitions and perpendicular transitions, respectively. Λ is the absolute value of the projection of the total electronic orbital angular momentum $\hat{\mathbf{L}}$ along the internuclear axis. $\mu_{ij}(R)$ is the electronic transition dipole moment between the neutral i and j states and $\mu_{iI}(R)$ is the transition dipole moment between the neutral i state of NO and the ionic $X\,^1\Sigma^+$ state of NO^+. The bound-state transition dipole moments $\mu_{ij}(R)$ are set as 0.1 a.u. (atomic units) and $\mu_{iI}(R) = \mu_{ij}(R)/20$ for ionization [66,67]. $E(t)$ is the electric field of the two-color pulse in Eq. (1), with Gaussian envelope

$$f_l(t) = \exp\left[-2\ln 2\left(\frac{t - t_{0l}}{T_l}\right)^2\right],$$

where t_{0l} denotes the central time, and T_l is the full width at half maximum (FWHM), $l = 1$ and 2 corresponding to the two-color pulses. In numerical simulations, the pulse intensities are $I_\omega = 2.2 \times 10^{13}$ W/cm^2 and $I_{2\omega} = 1.8 \times 10^{12}$ W/cm^2, and FWHMs are chosen as $T_\omega = 50$ fs and $T_{2\omega} = 60$ fs.

The AC Stark shift of Rydberg states in electric fields is added to the potential energy of all states except the ground $X\,^2\Pi$ and $B\,^2\Pi$ valence states. The shift is given by

$$E_{\text{shift}}(t) = \gamma U_p(t), \tag{9}$$

which is proportional to the ponderomotive energy $U_p(t)$ of a free electron in an oscillating electric field which is defined as [43–45]

$$U_p(t) = \sum_{l=1}^{2} \frac{e^2 E_{\omega_l}^2 f_l^2(t)}{4 m_e \omega_l^2}, \tag{10}$$

where $\omega_1 = \omega$ and $\omega_2 = 2\omega$, corresponding to the 800- and 400-nm laser fields. The ratio γ is a constant, $0 < \gamma < 1$, m_e the mass of electron, and e the elementary charge. It is found that the AC Stark shift on Rydberg states play a important role in the ATI spectrum. In these numerical simulations, the potential energy surfaces of the molecular electronic states are taken from Ref. [65]. The coupling between the $B\,^2\Pi$ and $C\,^2\Pi$ states is not considered in simulations because the effect of the two electronic state crossing is negligible in this multiphoton process.

The TDSE for NO is numerically solved for the nuclear wave functions with the sine discrete-variable representation (sine-DVR) [68,69], and Legendre basis function in combination of high-order split-operator propagation techniques [70,71]. The wave function along the R coordinate is represented by sine-DVR between $R_1 = 0.85$ Å and $R_2 = 3.8$ Å with 256 equally spaced points. The total propagation time is 3000 fs with a time step of 0.02 fs. The initial wave function is chosen as the ground rovibrational $|v, j\rangle = |0, 0\rangle$ of the $X\,^2\Pi$ state of the NO molecule. The photoelectron energy spectrum is calculated by integrating the wave function $\chi_{I,n}(R, \theta, t)$ of the the cation NO^+:

$$\mathcal{P}_I(E_n) = \lim_{t\to\infty} \int \sin\theta\, d\theta \int dR |\chi_{I,n}(R, \theta, t)|^2. \tag{11}$$

III. RESULTS AND DISCUSSIONS

The purpose of this work is to study coherent interference effects of vibration-electron states in vibrationally resolved molecular ATI spectra by two-color laser pulses. We use the molecule NO as a benchmark model to illustrate ultrafast molecular photoexcitation and photoionization processes. For the NO molecular system, the excited $A\,^2\Sigma^+$ and $B\,^2\Pi$ electronic state potentials are degenerate and cross [Fig. 1(b)], so the vibronic states are quasienergy degenerate. Therefore, a coherent superposition of the two excited electronic states is created by a multiphoton resonant excitation from the ground $X\,^2\Pi$ state with electronic configuration $\pi^4\pi^*$, to the $A\,^2\Sigma^+$ configuration $\pi^4\sigma^*$, and the $B\,^2\Pi$ configuration $\pi^3\pi^{*2}$. The $\pi^* - \sigma^*$ orbital transition to the $A\,^2\Sigma^+$ state produces little change in bond length whereas the $\pi - \pi^*$ orbital transition to the $B\,^2\Pi$ state results in a large bond length, i.e., large-R equilibrium. As a consequence of multiple pathway ionization, molecular ATI spectra exhibit interference patterns of the degenerate electronic states, which are functions of pulse phases, and photoelectron energies and emission angles. We measure experimentally photoionization yields and analyze these results by modeling theoretically electronic state interference effects. In the following, we first present and describe molecular photoelectron distributions and ATI spectra, and then study electronic state interference effects in multiple pathway ionization processes.

A. Molecular ATI spectra of NO

We measure molecular photoelectron momentum distributions by varying the relative phase $\Delta\phi$ in the presence of the two-color femtosecond laser pulses in Eq. (1). The pulse intensity and duration are fixed. Figure 2(a) presents the Abel inversed photoelectron distributions summed over the images taken from relative phase $\Delta\phi$ between -2π and 2π. The photoelectron energy spectrum obtained by integrating over the angular part is shown in Fig. 2(b), where the experimental data points are connected by solid lines. In order to understand the experimental observations, we also simulate the photoelectron energy spectrum by numerically solving TDSEs in Eq. (3), as shown in Fig. 2(c). It is found that the theoretical simulations are in good agreement with the experimental results. Of note is that the experimental energy spectra are broader than the simulated results because of the instrumental resolution and the volume-averaging effects within the laser focus.

Figure 2(a) shows that the two-dimensional (2D) photoelectron momentum (p_x, p_y) distribution is composed of three main momentum rings. In each main ring, there are several sub-rings. From Figs. 2(b) and 2(c) we find that three main peaks pK, K = 1–3, in Fig. 2(b) around energies 0.65, 2.2, and 3.75 eV with multiple subpeaks, as marked by vp$k$, k =

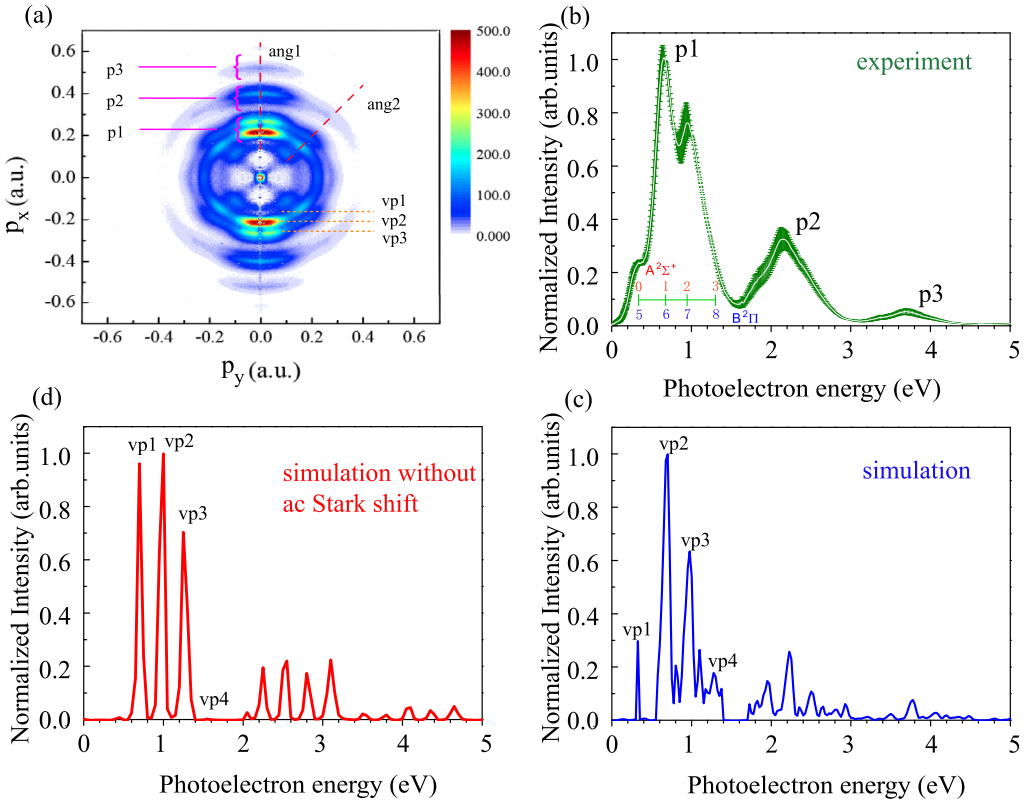

FIG. 2. (Upper row) Experimental observations of photoionization yields. (a) 2D photoelectron momentum (p_x, p_y) distributions in the molecule NO by the two-color femtosecond laser pulse [Eq. (1)]. (b) Molecular ATI spectra obtained by integrating over the angular part of the photoelectron distribution in (a). Peaks p1, p2, and p3 are the three lowest-order ATI in photoelectron spectra. (Bottom row) Numerical results of molecular ATI spectra in NO by numerically solving TDSEs in Eq. (3). (c) Simulations of ATI spectra including AC Stark shift effects in Eq. (14). Subpeaks vp1, vp2, vp3, and vp4 are the four vibrationally resolved photoelectron spectra in each ATI peak. (d) ATI spectra without considering the AC Stark shift effect are compared. The laser parameters are listed in the text.

1–4, in Fig. 2(c) are produced. The energy interval between the neighboring main peaks is 1.55 eV, corresponding to the 800-nm photon energy $\hbar\omega$, thus confirming the spectra as ATI spectra by absorption of $n\hbar\omega$ photons from the $A\,^2\Sigma^+$ and/or $B\,^2\Pi$ electronic states. As illustrated in Fig. 1(a), the molecule NO is excited from the ground $X\,^2\Pi$ electronic state to the excited $A\,^2\Sigma^+$ and $B\,^2\Pi$ electronic states by the two-color laser pulses, followed by ionization of the excited molecule via intermediate Rydberg states to the ground state of the molecular ion NO^+. As a consequence of multiphoton ionization, ATI spectra are obtained, as illustrated in Figs. 2(b) and 2(c).

The subpeaks vp$k$ at energies ε_k, $k = 1$–4, in each ATI peak pK, $K = 1$–3, in Fig. 2 reflect the vibrationally resolved photoelectron imaging of molecular coherent excitation processes. We simulate the time-dependent population in the two excited electronic states during the excitation and ionization processes to identify the vibrational levels. Figure 3 displays the evolution of the population in the excited $A\,^2\Sigma^+$ and $B\,^2\Pi$ electronic states, $\mathcal{P}^{A/B}(t)$, and their vibrational levels $v = 0$–8, $\mathcal{P}_v^{A/B}(t)$, with time. The corresponding populations are calculated from

$$\mathcal{P}^{A/B}(t) = \int \sin\theta\, d\theta \int dR |\chi_{A/B}(R,\theta,t)|^2 \qquad (12)$$

and

$$\mathcal{P}_v^{A/B}(t) = \int \sin\theta\, d\theta \int dR \left|\psi_v^{A/B}(R)\chi_{A/B}(R,\theta,t)\right|, \qquad (13)$$

where $\psi_v^{A/B}(R)$ is the eigenfunction of the vth vibration level in the $A\,^2\Sigma^+/B\,^2\Pi$ electronic state, and $\chi_{A/B}(R,\theta,t)$ is the time-dependent nuclear wave function of the $A\,^2\Sigma^+/B\,^2\Pi$ state obtained from the TDSE in Eq. (3). The corresponding maximum values of the population $\mathcal{P}_v^{A/B}(t)$ of the v vibrational level in the $A\,^2\Sigma^+$ and $B\,^2\Pi$ electronic states are listed in Table I. In the excitation and ionization processes, the populations in the two excited electronic states are comparable, thus enhancing electronic state interference effects. It is found that the time-dependent vibrational populations are sensitive to the molecular electronic symmetry during the excitation and ionization processes. For the $A\,^2\Sigma^+$ electronic state, the populations in the four lowest vibrational levels $v = 0$–3, $\mathcal{P}^A_{v=0-3}(t)$, are dominant, whereas for the $B\,^2\Pi$ state the populations mainly lie in the higher $v = 5$–8 vibration levels, i.e., $\mathcal{P}^B_{v=5-8}(t)$ dominate due to Franck-Condon factors. The evolution of the population with time illustrates the intermediate excitation process by the two-color laser pulse. As a result, one can conclude that the four subpeaks in ATI spectra come from the $v = 0$–3 vibrational levels of the $A\,^2\Sigma^+$ state and the $v = 5$–8 levels of the $B\,^2\Pi$ state, respectively. The quasiequal energy photoelectrons from the $A\,^2\Sigma^+$ and $B\,^2\Pi$

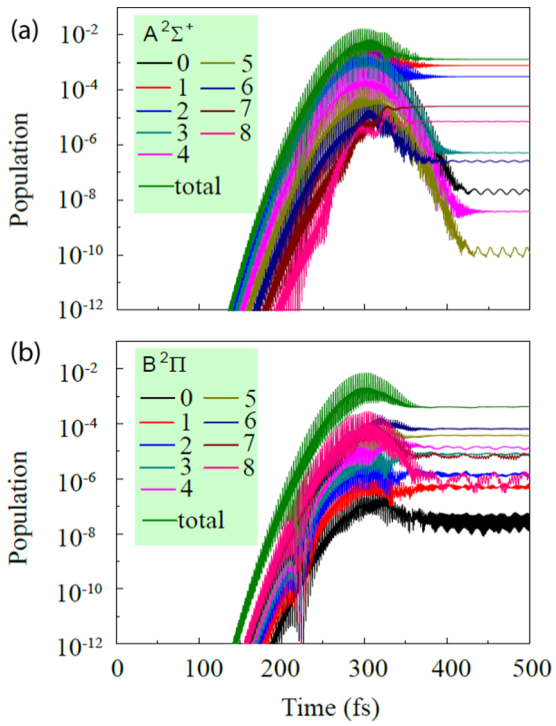

FIG. 3. Time-dependent population $\mathcal{P}_v^{A/B}(t)$ of the $v = 0$–8 vibrational level in the (a) $A\,^2\Sigma^+$ and (b) $B\,^2\Pi$ electronic states by two-color femtosecond laser pulses in Eq. (1) (cf. Fig. 2). The total population denotes $\mathcal{P}^{A/B}(t)$ in the $A\,^2\Sigma^+/B\,^2\Pi$ electronic states. The pulse intensities $I_\omega = 2.2 \times 10^{13}$ W/cm^2 and $I_{2\omega} = 1.8 \times 10^{12}$ W/cm^2, and the pulse FWHMs of $T_\omega = 50$ fs and $T_{2\omega} = 60$ fs are used.

electronic states interfere with each other in the continuum, leading to angular and kinetic energy-dependent interference patterns in ATI spectra, as discussed in the next section.

In Fig. 2(a) we see that the photoelectron momentum (p_x, p_y) distribution is mainly localized along the laser x polarization direction, noted as ang1. Moreover, a small part of the photoelectron distribution lies at the angle of about $\pm\pi/4$ with respect to the laser polarization, ang2. The photoelectron angular distribution illustrates the shape of the ionizing orbitals [72], i.e., the molecular orbitals of the natural electronic states, thus allowing to image electronic excitation [73]. For the $A\,^2\Sigma^+$ $\pi^4\sigma^*$ configuration and $B\,^2\Pi$ $\pi^3\pi^{*2}$ configuration, the maxima of the photoelectron angular distributions appear at 0 (ang1) and $\pm\pi/4$ (ang2), corresponding to the ionization of the σ^* (ang1) and π^* (ang2) due to the geometry of these orbitals [74]. The ground $X\,^2\Pi$ electronic state is a $\pi^4\pi^*$ configuration. In the nonoriented molecule, both parallel ($X\,^2\Pi$-$B\,^2\Pi$) and perpendicular ($X\,^2\Pi$-$A\,^2\Sigma^+$) transitions occur with linearly polarized laser pulses. As a result, the resonant excitation leads to a coherent superposition of the $A\,^2\Sigma^+$ and $B\,^2\Pi$ states due to $\pi^* - \sigma^*$ and $\pi - \pi^*$ excitation, resulting in photoelectron distributions localized at angles 0 and $\pi/4$.

TABLE I. The maximum values of the population $\mathcal{P}_v^{A/B}(t)$ of the $v = 1$–8 vibrational level in the $A\,^2\Sigma^+$ and $B\,^2\Pi$ electronic states by two-color femtosecond laser pulses. The pulse intensities $I_\omega = 2.2 \times 10^{13}$ W/cm^2 and $I_{2\omega} = 1.8 \times 10^{12}$ W/cm^2, and the pulse FWHMs of $T_\omega = 50$ fs and $T_{2\omega} = 60$ fs are used (cf. Fig. 3).

v	$A\,^2\Sigma^+$ ($\times 10^{-3}$)	$B\,^2\Pi$ ($\times 10^{-4}$)
0	3.115	6.108×10^{-3}
1	6.650	2.595×10^{-2}
2	5.577	9.753×10^{-2}
3	2.244	2.214×10^{-1}
4	6.433×10^{-1}	5.169×10^{-1}
5	1.298×10^{-1}	1.075
6	3.076×10^{-1}	2.075
7	2.819×10^{-1}	2.329
8	1.979×10^{-1}	2.857

Previous studies have shown that AC Stark shift effects of Rydberg states of NO can influence molecular photoelectron and fluorescence spectra [39,42–45]. We next present the molecular ATI process under the effects of AC Stark shift in the presence of the two-color laser pulse. At such pulse intensities, $I_\omega = 2.2 \times 10^{13}$ W/cm^2 and $I_{2\omega} = 1.8 \times 10^{12}$ W/cm^2, the corresponding ponderomotive energies of the electron is $U_p(\omega) = (eE_\omega)^2/4m_e\omega^2 = 1.32$ eV at 800 nm and $U_p(2\omega) = (eE_{2\omega})^2/4m_e(2\omega)^2 = 0.03$ eV at 400 nm, resulting in a maximum Stark shift in an oscillating electric field [44,75]. Of note is that in the two-color laser field, $U_p(2\omega)/U_p(\omega) = 0.023$, indicating that the ponderomotive energy $U_p(2\omega)$ induced by the 400-nm pulse is negligible. The shift of the photoelectron energy spectra is mainly caused by the 800-nm pulse. In order to exactly reproduce the photoelectron spectrum, a ratio of the AC Stark shift of the Rydberg resonant states to the ponderomotive energy $U_p(\omega)$ is introduced in the numerical simulations. The observed kinetic energy of the photoelectron is represented as [76]

$$\varepsilon_k = q\hbar\omega - (I_p - E_{v/v'}) - (1-\gamma)U_p(\omega), \qquad (14)$$

where $E_{v/v'}$ is the eigenenergy of the v/v' vibrational level in the $A\,^2\Sigma^+/B\,^2\Pi$ excited state, and the ratio γ is set as 0.75. By the 800-nm and 2.2×10^{13} W/cm^2 pulse a red-shift with energy 0.33 eV is induced. With such shift parameters in Eq. (14), the numerical simulations in Fig. 2(c) are in good agreement with the experimental results in Fig. 2(b), confirming the importance of the AC Stark shift effect in ATI processes.

The AC Stark effect can also influence the subpeaks in ATI spectra during molecular photoionization. In Fig. 2(d) we also present the simulation results of the photoelectron energy spectrum where the effect of the AC Stark shift is not considered. Comparing to the experimental observations in Fig. 2(b), one sees that the AC Stark effect strongly modifies the vibrationally resolved ATI spectra. A shift of 0.33 eV of the photoelectron spectrum occurs caused by the 800-nm pulse. The three main peaks, pK, $K = 1$–3, are localized at energies 0.98, 2.53, and 4.8 eV. The energy difference confirms the AC Stark shift effect. Of interest is that in each main ATI peak pK, the modulation of the amplitude of the subpeaks, vp$k$, $k = 1$–4, induced by the AC Stark effects is shown to be dependent on the photoelectron energy ε_k, i.e., the vibrational level in the excited $A\,^2\Sigma^+$ and $B\,^2\Pi$ states. For example, in Fig. 2(d), for the first main peak, p1, the amplitude of the subpeak vp1 at $\varepsilon_1 = 0.66$ eV is large whereas the subpeak

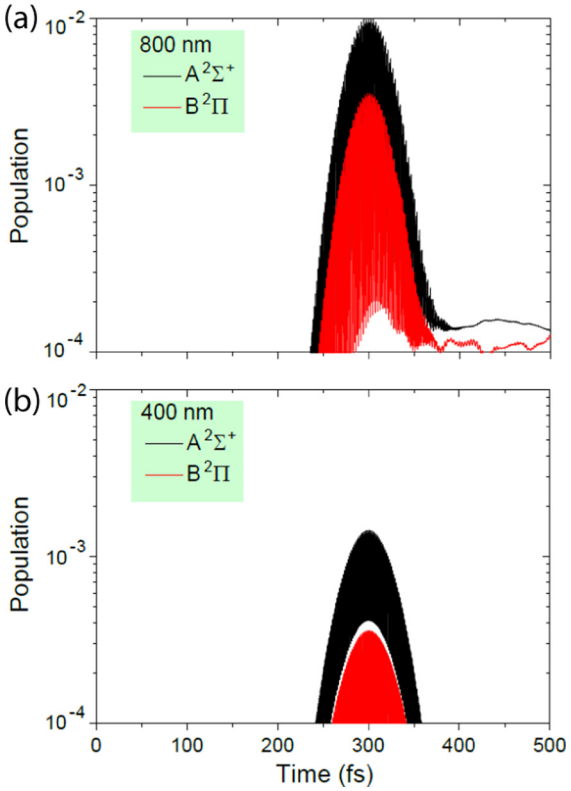

FIG. 4. Time-dependent population $\mathcal{P}^{A/B}(t)$ in the NO excited $A\,^2\Sigma^+$ and $B\,^2\Pi$ electronic states by (a) a single 800-nm (ω) pulse and (b) a 400-nm (2ω) laser pulse, respectively. The pulse intensities $I_\omega = 2.2 \times 10^{13}$ W/cm^2 and $I_{2\omega} = 1.8 \times 10^{12}$ W/cm^2, and the pulse FWHMs of $T_\omega = 50$ fs and $T_{2\omega} = 60$ fs are used.

vp4 at $\varepsilon_4 = 1.6$ eV is very weak. By considering the AC Stark shift effect, the subpeak vp1 is dramatically suppressed but the subpeak vp4 is enhanced in intensity, as shown in Fig. 2(c). Similar phenomena are obtained for the second (p2) and the third (p3) ATI peaks. The AC Stark shift of Rydberg states switches multiphoton ionization character of different vibrational levels of the $A\,^2\Sigma^+$ and $B\,^2\Pi$ electronic states from resonant to nonresonant or vice versa [39], therefore leading to enhancement and suppression of the photoelectron subpeaks in ATI spectra for different vibrational states.

B. Interference effects of electronic states in molecular ATI

We next present the coherent interference effect of electronic states in the ATI spectra of the molecule NO by the phase-controlled two-color femtosecond laser pulse in Eq. (1). In order to describe the excitation channel, we simulate two multiphoton excitation processes by a 800-nm and a 400-nm pulse, separately. Figure 4 displays the evolutions of the population $\mathcal{P}^{A/B}(t)$ obtained from Eq. (12) in the two excited (black lines) $A^2\Sigma^+$ and (red lines) $B\,^2\Pi$ electronic states with time. The laser pulses at (a) 800 and (b) 400 nm are used, and the other parameters are the same as in Fig. 2. Comparisons of these results in Fig. 4 show that the transition populations induced by the 400-nm pulse [Fig. 4(b)] are much weaker than those by the 800-nm pulse [Fig. 4(a)], with a factor of approximately $\frac{1}{10}$. Therefore, we can conclude that the multiple channel excitation effects by the 800- and 400-nm pulses together or the 400-nm pulse solely are negligible. The population transition from the ground $X\,^2\Pi$ state to the two excited $A\,^2\Sigma^+$ and $B\,^2\Pi$ electronic states mainly arises from a four ω (800-nm) photon resonant excitation. As a result, a superposition state of the $A\,^2\Sigma^+$ and $B\,^2\Pi$ electronic states is created. The corresponding wave function $\psi_c(\mathbf{R})$ reads as

$$\psi_c(\mathbf{R}, t) = \psi_A(\mathbf{R}, t) + \psi_B(\mathbf{R}, t), \tag{15}$$

where the two molecular wave functions define as $\psi_A(\boldsymbol{R}, t) = \sum_{vjm} c_{vjm}(t)\psi_v(R)\psi_{jm}(\theta, \phi)e^{-iE_{vjm}t/\hbar}$ is for the $A\,^2\Sigma^+$ electronic state and $\psi_B(\boldsymbol{R}, t) = \sum_{v'j'm'} c_{v'j'm'}(t)\psi_{v'}(R)\psi_{j'm'}(\theta, \phi)e^{-iE_{v'j'm'}t/\hbar}$ is for the $B\,^2\Pi$ state. $\psi_{v/v'}(R)$ and $\psi_{jm/j'm'}(\theta, \phi)$ are the wave functions of the vibrational v/v' and rotational $jm/j'm'$ stationary states with total eigenenergies $E_{vjm/v'j'm'}$, respectively. $c_{vjm}(t)$ and $c_{v'j'm'}(t)$ are the occupation coefficients of the v/v' vibrational levels in the two electronic states determined by the intensity of the driving laser pulse. Moreover, the two $A\,^2\Sigma^+$ and $B\,^2\Pi$ states are coupled weakly by negligible nonadiabatic rotational coupling with a crossing of their electronic potentials at $R \approxeq 1.2$ Å corresponding to equilibrium of the ground state. We therefore focus on the coherent superposition created by the four ω resonant excitations.

To monitor the coherent electronic-vibrational coupling of the molecule NO in Eq. (15), we theoretically model and analyze photoionization yields measured experimentally in the presence of the two-color laser femtosecond pulse. As illustrated in Fig. 1(b), after absorption of four ω photons, the excited molecule NO is ionized simultaneously via multiphoton resonance with Rydberg states from the coherent state $\psi_c(\mathbf{R}, t)$ shown in Eq. (15) to the ionic $X\,^1\Sigma^+$ state of NO^+, by the two-color laser pulse, thus giving rise to ATI spectra in Fig. 2. The two excited $A\,^2\Sigma^+$ and $B\,^2\Pi$ states are degenerate with quasiequal vibrational energies. Consequently, the ionized electron wave packets in the continuum from the two electronic states by multiphoton transitions have the same kinetic energies, resulting in the interference effects in produced ATI spectra. In order to identify the interference effects of electronic states, we compare theoretically two photoionization processes by the two-color femtosecond pulses where the excited $A\,^2\Sigma^+$ and $B\,^2\Pi$ electronic states are not included, respectively. Figure 5 displays the corresponding results of molecular ATI spectra obtained by numerically solving TDSEs in Eq. (3). In these two cases, the excitation and ionization processes can be regarded as two pathways: (green dashed line) $X\,^1\Sigma^+ \leftarrow A\,^2\Sigma^+ \leftarrow X\,^2\Pi$ and (red dot line) $X\,^1\Sigma^+ \leftarrow B\,^2\Pi \leftarrow X\,^2\Pi$. The two ionization processes are independent. For comparison, we also plot (blue solid line) the results of ATI spectra in which both the two-electron states are involved, as presented in Fig. 2. Since we here only consider the effects of interference patterns on the photoelectron kinetic energy, the results are obtained by integrating over the variables of the relative phase $\Delta\phi$ and the emission angle.

From Fig. 5 one sees that the total ATI spectral amplitudes are not simply the sum of those of the photoionization yields separately arising from the $A\,^2\Sigma^+$ and $B\,^2\Pi$ states. For examples, for the vp2 peak, the total spectral amplitude is larger than the sum of the cases without the $A\,^2\Sigma^+$ and $B\,^2\Pi$

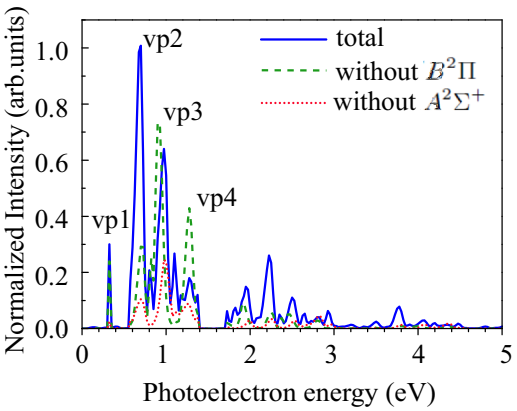

FIG. 5. Molecular ATI spectra of NO simulated by numerically solving TDSEs in Eq. (3) by intense two-color pulses at intensities $I_\omega = 2.2 \times 10^{13}\,\mathrm{W/cm^2}$ and $I_{2\omega} = 1.8 \times 10^{12}\,\mathrm{W/cm^2}$, and the pulse FWHMs of $T_\omega = 50$ fs and $T_{2\omega} = 60$ fs. To illustrate the interference effects of electronic states, the results obtained without the (green dashed line) excited $B\,^2\Pi$ or (red dot line) $A\,^2\Sigma^+$ states are also compared. Total (blue solid line) denotes the result in which both the $A\,^2\Sigma^+$ and $B\,^2\Pi$ electronic states are involved.

electronic states, whereas for the vp4 peak a reverse process occurs. The difference indicates the constructive and destructive interference effects of the two electronic states. The coupling of the two ionization channels, $X\,^1\Sigma^+ \leftarrow A\,^2\Sigma^+$ and $X\,^1\Sigma^+ \leftarrow B\,^2\Pi$, leads to interference effects. Moreover, each ionization channel from the excited $A\,^2\Sigma^+$ and $B\,^2\Pi$ electronic state by the two-color laser pulse is composed of multiple pathways. For example, the first ATI peak p1 arises from four ionization pathways by absorbing three $\omega+\omega+\omega$ photons and two $\omega+2\omega$ photons from the two electronic states, respectively. The coherent electron wave packets in the continuum with the same kinetic energies interfere with each other. We analyze the electronic state interference model in multipathway ATI processes based on the perturbation theory [77–79]. As derived in the Appendix, the total transition probability $P^{\mathrm{total}}(\varepsilon_k)$ is the square of the two amplitudes $P^{3\omega}(\varepsilon_k)$ and $P^{2\omega+\omega}(\varepsilon_k)$ with an interference term via the cross products of the three- and two-photon ionization amplitudes $P^I_{\mathrm{int}}(\varepsilon_k)$ from, respectively, the $A\,^2\Sigma^+$ and $B\,^2\Pi$ electronic states, i.e.,

$$P^{\mathrm{total}}(\varepsilon_k) = \sum_{i=A,B} \left[P_i^{3\omega}(\varepsilon_k) + P_i^{2\omega+\omega}(\varepsilon_k)\right] + P^I_{\mathrm{int}}(\varepsilon_k). \quad (16)$$

The interference term of the photoelectron spectrum is proportional to the transition coefficient $\alpha(\varepsilon_k)$ of the three- and two-photon processes, as predicted in Eq. (A9), i.e.,

$$P^I_{\mathrm{int}}(\varepsilon_k) \sim \alpha_0 + \alpha_1 e^{-\alpha_2 \varepsilon_k^2}, \quad (17)$$

where α_i, $i = 0$, 1, and 2, are coefficients of ionization processes which are determined by the driving pulse. Therefore, at different kinetic energies ε_k, the photoelectron spectra exhibit different interference patterns, as displayed in Fig. 5. The theoretical model in Eq. (17) describes qualitatively the numerical simulations.

As shown in Fig. 5, for the subpeaks vp1 and vp2 at energies $\varepsilon_1 = 0.33$ eV and $\varepsilon_2 = 0.64$ eV, constructive interference occurs. The amplitudes of the total ATI spectra are approximately the sum of those of the cases without the $A\,^2\Sigma^+$ or $B\,^2\Pi$ states. However, for the subpeaks vp3 and vp4 at energies $\varepsilon_3 = 0.95$ eV and $\varepsilon_4 = 1.27$ eV, the photoionization from the $A\,^2\Sigma^+$ and $B\,^2\Pi$ electronic states exhibits destructive interference patterns where the total ATI spectral amplitudes are nearly the difference between the two single excited state processes. The energy ε_k (subpeak) dependence of ATI spectral amplitudes illustrates the vibrationally resolved interference effects. The Rydberg states induce different resonance and nonresonance multiphoton ionizations from various vibrational levels of the $A\,^2\Sigma^+$ and $B\,^2\Pi$ electronic states. The coefficients α_i, i.e., the transition matrix elements $T^{A/B}_{2/3}$ (in the Appendix), are different. As a result, interference effects are shown to be sensitive to the photoelectron energy ε_k (subpeak) in ATI spectra. Similar phenomena of the ε_k-dependent interference are also obtained in higher-order ATI peaks p2 and p3, which can be described based on the multiple pathway ionization interference model derived in the Appendix.

The vibrationally resolved interference of electronic states, the $A\,^2\Sigma^+$ and $B\,^2\Pi$ states, is also dependent on the relative phase $\Delta\phi$ by the two-color laser pulses. Figure 6(a) shows the experimental measurements of the dependence of the ATI spectra on the relative phase $\Delta\phi$ for the three subpeaks vp1–3 at photoelectron kinetic energies $\varepsilon_{1-3} = 0.33$, 0.64, and 0.95 eV. We vary the relative phase $\Delta\phi$ from -2π to 2π and integrate the angular part of photoelectron momentum distributions in Fig. 2(a). The phase dependence at the three subpeaks $\mathrm{vp1}_3$ are also displayed separately in Fig. 6(b). Results show periodical oscillations with the relative phase $\Delta\phi$ for the three subpeaks. The maxima and minima occur at $\Delta\phi \sim (2n \pm 1)\pi$ and $2n\pi$, $n = 0, \pm1, \pm2, \ldots$. In Fig. 6(c) we also display numerical simulations obtained from TDSEs. Similar results are reproduced, confirming the dependence of the electron interference on the relative phase $\Delta\phi$ and the photoelectron energy.

In Fig. 7 we show the dependence of the vibrationally resolved ATI spectra on the emission angle of photoelectron. We consider again the cases for the three lowest subpeaks vp1–3 at energies $\varepsilon_{1-3} = 0.33$, 0.64, and 0.95 eV, as in Fig. 6. Figures 7(a)–7(d) present experimental measurements. We also plot the numerical results in Fig. 7(e) which is in agreement with the experimental observation in Fig. 7(d) for both emission angles. From Fig. 7, one sees that the dependence is sensitive to the emission angles of photoelectron. As shown in experimental measurements in Fig. 7(d), at the angle $45^\circ \pm 15^\circ$ (30°–60°, ang2), varying the relative phase $\Delta\phi$ leads to a slight variance, around $\Delta\phi = -1.05\pi \pm 0.05\pi$. However, at the angle $0 \pm 20^\circ$ (0°–20°, ang1), the result shows a dramatic oscillation. For the first subpeak vp1, the maximum appears at $\Delta\phi \approx -1.05\pi$. As the photoelectron energy increases, the relative phase $\Delta\phi$ increases and then decreases. For the subpeaks vp2 and vp3, one obtains the maxima at $\Delta\phi = -0.8\pi$ and -1.11π.

The relative phase $\Delta\phi$ dependence reflects the interference of the multiple pathway ionization induced by the two-color pulse, and the emission angle dependence corresponds to the two channels of molecules ionized from the $A\,^2\Sigma^+$ and $B\,^2\Pi$ electronic states with $\pi^4\sigma^*$ and $\pi^3\pi^{*2}$ configurations. These ionization channels interfere with each other as well. As shown in he Appendix, the combination of the two

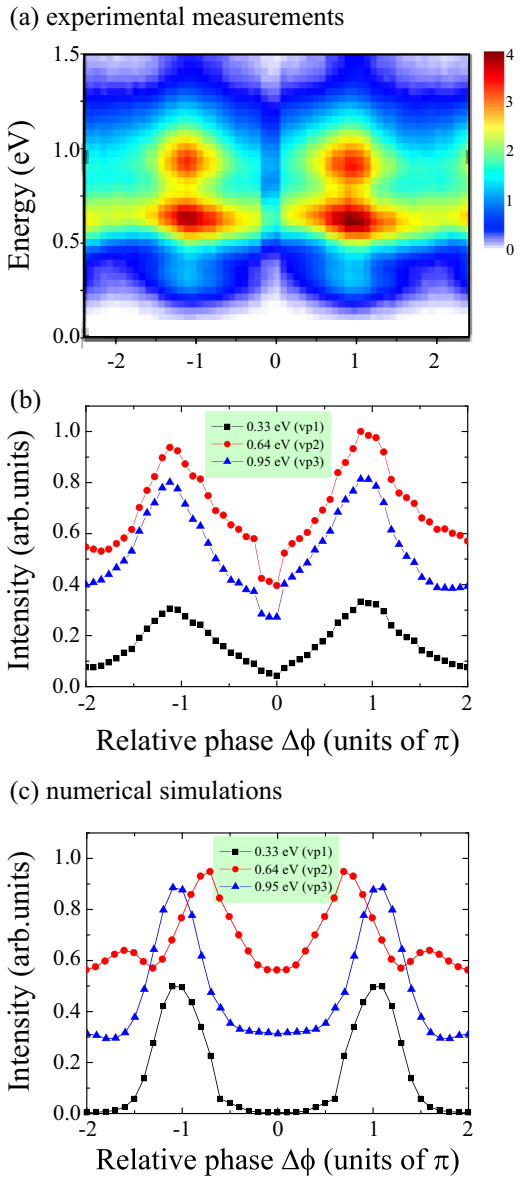

FIG. 6. Dependence of ATI spectra for the first ATI peak, p1, on the relative pulse phase $\Delta\phi$ and the subpeak energies ε_k by two-color pulses. (a), (b) Experimental measurements and (c) numerical simulations.

multipathway ionization leads to ATI distributions as functions of the pulse relative phase and the photoelectron energy and emission angle. According to the electronic state interference model in multipathway photoionization processes, the photoelectron distribution for the first ATI peak p1 is given by

$$P^{I}_{\rm int}(\varepsilon_k, \theta, \Delta\phi) = \alpha_{32}(\varepsilon_k)\cos(\theta - \Delta\phi), \tag{18}$$

where $\alpha_{32} = \alpha_0 + \alpha_1 e^{-\alpha_2\varepsilon_k^2}$ are the coefficients of the two- and three-photon processes, the same as in Eq. (17) and θ denotes the angle between the directions of the emitted photoelectron and the laser polarization aixs.

From Eq. (18) we see that the interference term $P^{I}_{\rm int}(\varepsilon_k, \theta, \Delta\phi)$ of the photoelectron angular distribution is a cosine triangular function of the relative phase with the form $\cos(\theta - \Delta\phi)$. Therefore, the interference patterns in Fig. 6 show 2π periodic oscillation with the relative phase $\Delta\phi$. Due to the effects of the electronic coherent interference, the interference is modulated by the energy differences ε_k, with a function of $\alpha_1 e^{-\alpha_2\varepsilon_k^2}$. The variation of ε_k results in a modulation of the multiple pathway ionization interference. Consequently, increasing the photoelectron kinetic energy varies the relative phase $\Delta\phi$-dependent interference patterns.

As predicted in Eq. (18), at different photoelectron emission angles, the relative phase $\Delta\phi$-dependent interference patterns shift with an angle θ. The prediction, however, slightly differs from our measurements in Fig. 7. For example, for the subpeak vp2 in Fig. 7(b), the maximum of the dependence predicted from the theoretical model occurs at $\theta - \Delta\phi = n\pi$, whereas the measured results exhibit a nonlinear process. The difference corresponds to the different ionization angle of the $A\,^2\Sigma^+$ and $B\,^2\Pi$ states. In the interference model of electronic states in the Appendix, the same initial molecular orbitals are assumed. However, in the molecular NO ionization processes, the angular distribution corresponds to the perpendicular and parallel ionization processes from the $A\,^2\Sigma^+$ and $B\,^2\Pi$ electronic states with different orbital symmetries σ^* and π^*. Due to the effects of the intermediate Rydberg states, the ionization coefficients α_i depend on both the photoelectron emission angle and kinetic energies, i.e., $\alpha_i(\varepsilon_k, \theta)$. The relative phase $\Delta\phi$ dependence at different photoelectron kinetic energies ε_k is modulated by the photoelectron emission angle. Photoelectron spectra at various photoelectron energies ε_k and emission angles therefore show different dependencies on the relative phase $\Delta\phi$ of pulses. One then has the modified interference model

$$P^{I}_{\rm int}(\varepsilon_k, \theta, \Delta\phi) \sim \alpha_{32}(\varepsilon_k, \theta)\cos(\theta - \Delta\phi). \tag{19}$$

As shown in Fig. 7, the photoelectron distribution at the angle 45° (ang2) results from the π^* orbital transitions. Their interference effects lead to a strong modulation of the phase $\Delta\phi$ dependence. At the angle 0 (ang1), the perpendicular process becomes weak and the parallel (σ^*) transition dominates. As a result, the interference effect of electronic states suppresses and the dependence varies slightly with the relative phase $\Delta\phi$.

Similar phenomena of electronic state interference effects can be obtained in higher-order ATI spectra. For the second ATI peak, p2, the molecule is ionized via six pathways, i.e., four $\omega+\omega+\omega+\omega$, three $\omega+\omega+2\omega$, and two $2\omega+2\omega$ photon absorptions, started respectively from the $A\,^2\Sigma^+$ and $B\,^2\Pi$ electronic states. The multiple pathway ionization is composed of the contributions from the six channels and their interference terms. According to the interference model in the Appendix, the interference term then can be given by

$$P^{II}_{\rm int}(\varepsilon_k, \theta, \Delta\phi) = [\alpha_{43}(\varepsilon_k, \theta) + \alpha_{32}(\varepsilon_k, \theta)]\cos(\theta - \Delta\phi) + \alpha_{42}(\varepsilon_k, \theta)\cos^2(\theta - \Delta\phi). \tag{20}$$

One also sees that the third ATI peak, p3, arises from six pathway transitions after direct absorptions of five ω photons $\omega+\omega+\omega+\omega+\omega$, and three ω and one 2ω photons, $\omega+\omega+\omega+2\omega$, and one ω and two 2ω photons, $\omega+2\omega+2\omega$, initiated from the $A\,^2\Sigma^+$ and $B\,^2\Pi$ electronic states. The interference term of photoelectron distributions can be

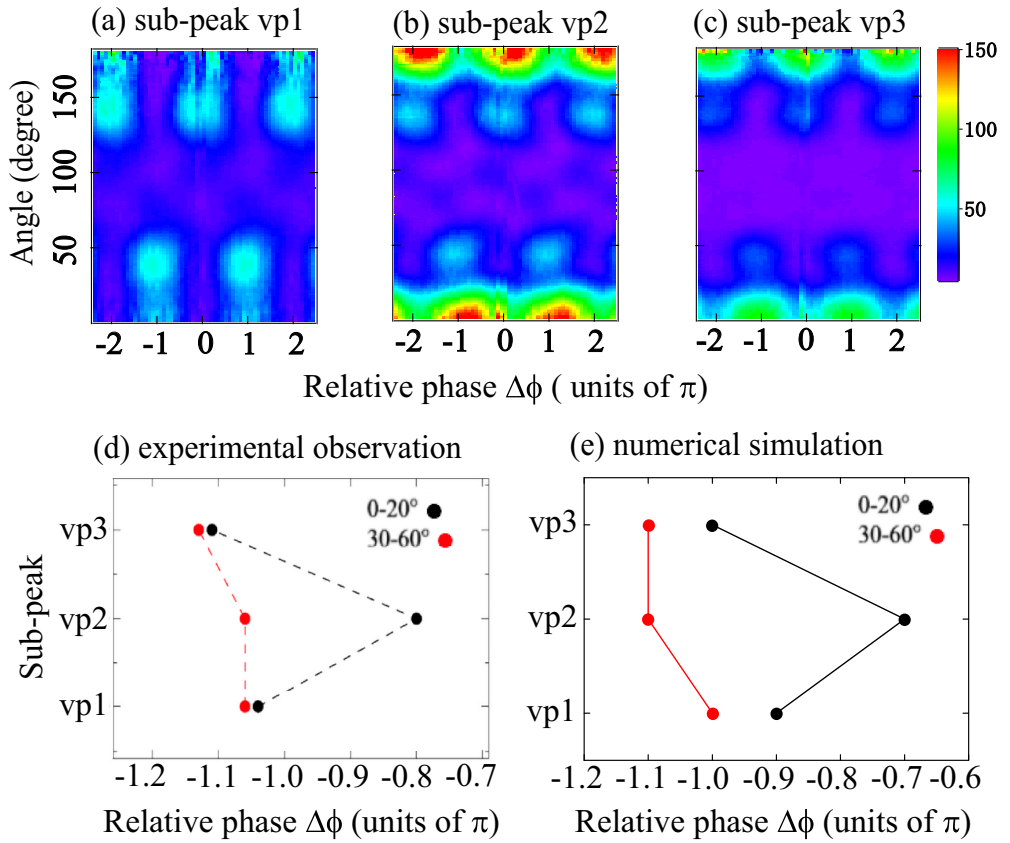

FIG. 7. (Upper row) Experimental measurements of emission angle and relative phase $\Delta\phi$-dependent photoelectron distributions at energies (a) $\varepsilon_1 = 0.33$ eV, subpeak vp1, (b) $\varepsilon_2 = 0.64$ eV, subpeak vp2, and (c) $\varepsilon_3 = 0.95$ eV, subpeak vp3. (Bottom row) The maxima in (a)–(c) at angles $0^\circ \pm 20^\circ$ (black dots, 0°–20°, ang1) and $45^\circ \pm 15^\circ$ (red dots, 30°–60°, ang2) vs the relative phase $\Delta\phi$ are obtained by (d) experimental observations extracted from (a)–(c) and (e) numerical simulations calculated from TDSEs.

expressed as

$$P_{\rm int}^{III}(\varepsilon_k, \theta, \Delta\phi) = [\alpha_{54}(\varepsilon_k, \theta) + \alpha_{43}(\varepsilon_k, \theta)]\cos(\theta - \Delta\phi) + \alpha_{53}(\varepsilon_k, \theta)\cos^2(\theta - \Delta\phi). \quad (21)$$

The interference patterns in Eqs. (20) and (21) contain both $\cos^2(\theta - \Delta\phi)$ and $\cos(\theta - \Delta\phi)$ terms.

To verify the multiple pathway ionization interference of electronic states for molecular ATI in Eqs. (20) and (21), we show experimental measurements and numerical simulations in Fig. 8 for the two higher-order ATI peaks p2 and p3 marked in Fig. 2. The results show similar dependence on the relative phase $\Delta\phi$ and photoelectron kinetic energy ε_k, as those for the first ATI peak p1 in Fig. 6. The maxima appear around the phase $\Delta\phi \sim \pm\pi$ which depend on the photoelectron kinetic energies. The distributions oscillate periodically for each subpeak vp$k$ at energy ε_k, $k = 1$, 2, and 3. However, for the subpeaks at higher energies, the dependence is also modulated. As shown in Fig. 8 for the numerical simulations (right column), around the relative phases 0 and 2π, humps with small amplitudes are produced (red and blue lines). The modulation mainly results from the $\cos^2(\theta - \Delta\phi)$ interference term in Eqs. (20) and (21).

In Fig. 8, one notes that in the experimental measurements, the ATI spectra show dominant distributions around the relative phase $\Delta\phi \sim \pm\pi$. The small humps around $\Delta\phi \sim 2n\pi$ predicted by our numerical simulations, however, can not be observed experimentally. As discussed in Fig. 4, the population transition by absorbing two $2\omega + 2\omega$ photons is very weak. In the two-color laser fields, the multiple ω photon excitation and ionization dominates. In the six-pathway ionization processes, the coefficients $\alpha_{42}(\varepsilon_k, \theta)$ and $\alpha_{32}(\varepsilon_k, \theta)$ in Eq. (20) and $\alpha_{53}(\varepsilon_k, \theta)$ and $\alpha_{43}(\varepsilon_k, \theta)$ in Eq. (21) are very small and difficult to measure in experiments. Therefore, the interference patterns then can be reduced simply to

$$P_{\rm int}^{II'}(\varepsilon_k, \theta, \Delta\phi) = \alpha_{43}(\varepsilon_k, \theta)\cos(\theta - \Delta\phi) \quad (22)$$

for the second ATI peak p2, and

$$P_{\rm int}^{III'}(\varepsilon_k, \theta, \Delta\phi) = \alpha_{54}(\varepsilon_k, \theta)\cos(\theta - \Delta\phi) \quad (23)$$

for the third ATI peak p3. The three ATI peaks have similar interference patterns, following the form of $\alpha(\varepsilon_k, \theta)\cos(\theta - \Delta\phi)$ in Eqs. (18), (22), and (23). Consequently, in Figs. 6 and 8, we measure experimentally similar dependence of the electronic state interference on the relative phase $\Delta\phi$ and photoelectron kinetic energy in molecular ATI spectra.

Of note is that in this work we present phase-controlled two-color ATI processes with strong intensity of 800-nm and weak intensity of 400-nm pulses, $I_{2\omega}/I_\omega \approx 1/10$. The weak 400-nm pulse serves as a control field to modulate the multiphoton ionization from the $A^2\Sigma^+$ and $B^2\Pi$ electronic

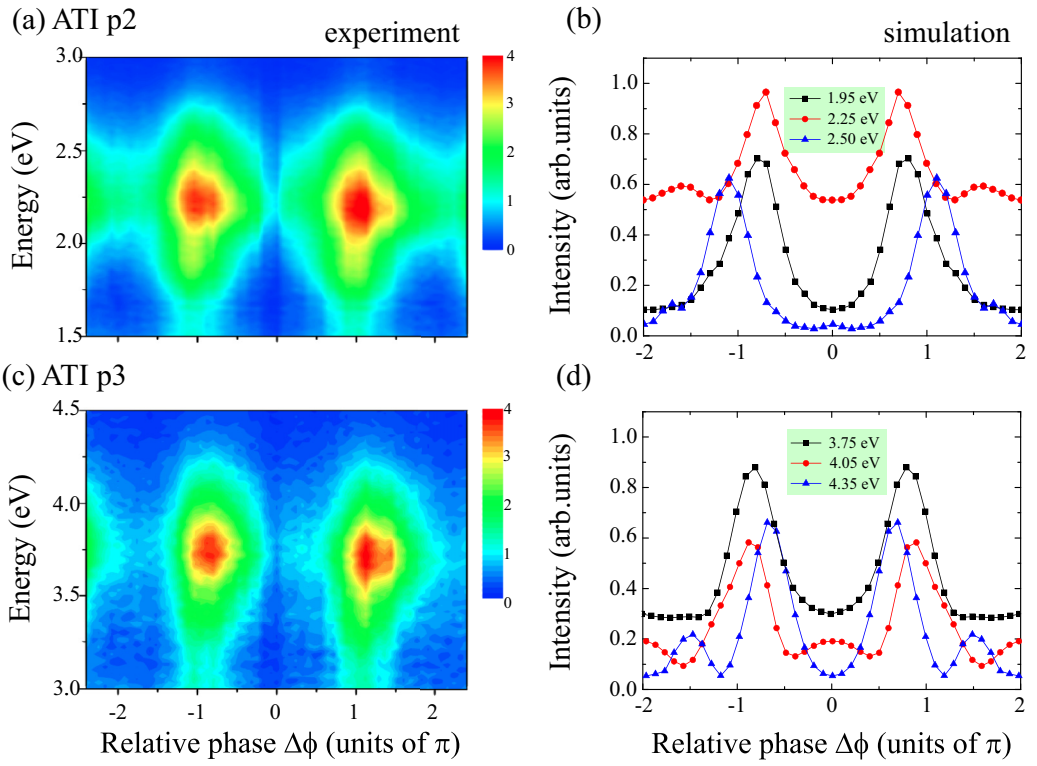

FIG. 8. Dependence of the electronic state interference on the relative phase $\Delta\phi$ between the two-color pulses for [top row: (a), (b)] the second ATI peak 2 at various energies $\varepsilon_{1-3} = 1.95$, 2.25, and 2.50 eV, and [bottom row: (c), (d)] the third ATI peak 3 at 3.75, 4.05, and 4.35 eV. [Left column: (a), (c)] Experimental measurements and [right column: (b), (d)] numerical simulations.

states, thus giving rise to multiple channel photoionization interference effects in ATI spectra in Figs. 6–8. For the converse scheme with strong 400- and weak 800-nm pulses which has been used to study for example strong field RABBITT [80–82], similar interference phenomena should be produced, as we predict in Eqs. (A8), (A16), and (A23).

IV. CONCLUSIONS

In summary, vibrationally resolved ATI spectra in the molecule NO by intense phase-controlled two-color femtosecond laser pulses have been studied. We measure experimentally and model theoretically molecular photoionization yields to explore coherent interference effects between quasiequal energy electronic-vibrational states. It is found that the photoelectron distribution in the ATI of NO is a function of the relative phase between the two-color pulses, the photoelectron kinetic energy and emission angle. Two excited electronic states are coherently combined by ultrafast pulses, from which multiple pathway ionization leads to interference patterns in ATI. Numerical simulations from molecular TDSEs and theoretical analysis of the multiple pathway ionization interference model confirm the experimental observations.

We find that ATI spectral peaks exhibit multiple subpeaks arising from various vibrational levels of the two coherent electronic $A\,^2\Sigma^+$ and $B\,^2\Pi$ states, which are strongly influenced by the AC Stark effect. The interference effects between the two electronic states can also modulate the ATI spectra. Different constructive and destructive interference patterns are obtained in these subpeaks. The phenomenon results from intermediate Rydberg states which cause resonant and nonresonant multiphoton ionization. The vibrational resolved interference patterns in ATI spectra are dependent on the emission angle of photoelectron, reflecting the initial molecular orbitals. By the two-color laser pulse, multiple channel ionization processes give rise to relative phase-dependent interference patterns in ATI spectra. It is also found that in the first ATI peak, p1, the interference pattern approximately follows the form $\alpha(\varepsilon_k,\theta)\cos(\theta-\Delta\phi)$ [Eq. (19) and Fig. 7]. For higher-order ATI peaks, it becomes more complex. The interference patterns contain both $\cos^2(\theta-\Delta\phi)$ and $\cos(\theta-\Delta\phi)$ terms, as shown in Eqs. (20) and (21) and Fig. 8, for peaks p2 and p3. Of note is that the two 2ω transitions are very weak, thus leading to the small amplitudes of the interference term $\cos^2(\theta-\Delta\phi)$. As a result, the corresponding interference hump can not be observed in experimental measurements, as shown in Fig. 8.

Our results show that electronic-vibrational state coherence can be monitored from photoelectron interference patterns in molecular ATI spectra produced by intense phase-controlled two-color femtosecond laser pulses. The photoelectron distribution results from the interference effects between the two coherently prepared electronic states in combination with multiple multiphoton ionization processes. The ATI spectra encode the information of the vibrational level and the orbital symmetry of electronic states and the pulse relative phase. The modification of photoelectron patterns illustrates the electron coherence via electronic-vibrational state interference. This work presents a scheme to monitor electronic-vibrational state interference with various orbital symmetries, and thus

provides a way to explore and reconstruct coherent electron excitation processes in molecules by ultrashort laser pulses. The sensitivity of the interference patterns to the phase makes them a possible means of characterizing these pulses. The developments of ultrafast laser technology [83,84] allow to extend the method for exploring intramolecular coherent electronic dynamics on its natural timescale in molecular reactions [85,86], which therefore demonstrate a great potential for ultrafast photoelectron imaging in more complex molecular systems.

ACKNOWLEDGMENTS

This work was supported by National Natural Science Foundation of China (NNSFC) (Grants No. 11704148, No. 11534004, No. 11627807, No. 21222308, No. 21133006, and No. 21433009) and the China Postdoctoral Science Foundation (Grant No. 2015M571336). K.-J.Y. and A.D.B. thank NSERC and FQRNT for their support.

Y.L. and W.H. contributed equally to this work.

APPENDIX: MOLECULAR ELECTRONIC STATE INTERFERENCE MODELS IN MULTIPLE PATHWAY ABOVE-THRESHOLD IONIZATION PROCESSES

We present the interference of electronic states in multiple pathway photoionization processes based on perturbation theory [77–79]. The ionization initiates from two coherent electronic $A\,^2\Sigma^+$ and $B\,^2\Pi$ states of molecules by two-color $\omega_1 = \omega$ and $\omega_2 = 2\omega$ pulses. Such bichromatic laser pulse can produce photoelectron wave packets with the same kinetic energies by combination of multiple multiphoton transitions and steer them through different pathways in the continuum, thus creating the interference effects in the photoelectron spectra. The interference model depends on the ATI peaks.

For the first peak in ATI spectra, two ionization pathways occur from the $A\,^2\Sigma^+$ (A) and $B\,^2\Pi$ (B) states after absorptions of three ω_1 photons and two photons (i.e., $\omega + 2\omega$). The first-order amplitude $P^{3\omega_1}_{A/B}(\varepsilon_k)$ for $3\omega_1$ photon ionization from the A/B state of the molecule NO by the electric field $E_\omega(t)$ is defined by [4,87]

$$P^{3\omega_1}_{A/B}(\varepsilon_k, t) = \frac{\langle\psi_i(\varepsilon_k)|\mu_{A/B}E_\omega(t)|\psi_2\rangle\langle\psi_2|\mu_{A/B}E_\omega(t)|\psi_1\rangle\langle\psi_1|\mu_{A/B}E_\omega(t)|\psi_{A/B}\rangle}{(E_{A/B} - E_2 + 2\omega)(E_{A/B} - E_1 + \omega)}. \tag{A1}$$

$\psi_{A/B}$ is the initial state of the molecule NO with energy $E_{A/B}$, in Eq. (15) and ψ_i is the final state, i.e, the continuum in NO^+. $\psi_{1/2}$ denotes the intermediate state with energy $E_{1/2}$, and ε_k is the photoelectron kinetic energy. $\mu_{A/B}$ presents the transition dipole moment of the target. The field-molecule interaction is given by

$$\mu_{A/B}E_\omega(t) = \mu_{A/B}E_\omega f(t)e^{-i\omega t}e^{-i\theta}. \tag{A2}$$

θ is the angle between the electric field and the transition dipole direction (the molecular axis). The amplitude $P^{\omega_1+\omega_2}_{A/B}(\varepsilon_k, t)$ for the $\omega_1 + \omega_2$ photoionization from the A/B state of the molecule NO by the electric fields $E_\omega(t)$ and $E_{2\omega}(t)$ is defined by

$$P^{\omega_1+\omega_2}_{A/B}(\varepsilon_k, t) = \frac{\langle\psi_i(\varepsilon_k)|\mu_{A/B}E_{2\omega}(t)|\psi_1\rangle\langle\psi_1|\mu_{A/B}E_\omega(t)|\psi_{A/B}\rangle}{E_{A/B} - E_1 + \omega} + \frac{\langle\psi_i(\varepsilon_k)|\mu_{A/B}E_\omega(t)|\psi_2\rangle\langle\psi_2|\mu_{A/B}E_{2\omega(t)}|\psi_{A/B}\rangle}{E_{A/B} - E_2 + 2\omega}, \tag{A3}$$

with the interaction term

$$\mu_{A/B}E_{2\omega}(t) = \mu_{A/B}E_{2\omega}f(t)e^{-i(2\omega t+\Delta\phi)}e^{-i\theta} \tag{A4}$$

since the unit vector $\mu_0 e_0 = e^{i\theta}$. The total transition probability is the square of these amplitudes, which is insensitive to the angle θ, the phase difference $\Delta\phi$, and time t, and an interference term $P^I_{\rm int}(\varepsilon_k, t)$ via the cross products of the three- and two-photon ionization amplitudes. The interference term can be simply written as

$$P^I_{\rm int}(\varepsilon_k, t) = \left[P^{3\omega_1}_A(\varepsilon_k, t) + P^{3\omega_1}_B(\varepsilon_k, t)\right]^*\left[P^{\omega_1+\omega_2}_A(\varepsilon_k, t) + P^{\omega_1+\omega_2}_B(\varepsilon_k, t)\right] + \text{c.c.} \tag{A5}$$

Submitting Eqs. (A1)– (A4) into Eq. (A5) one then obtains the interference term

$$\begin{aligned} P^I_{\rm int}(\varepsilon_k, \theta, \Delta\phi, t) = E^4_\omega E_{2\omega} f^5(t)\big[&\left(T^A_3 T^A_2 + T^B_3 T^B_2\right)\cos(\theta - \Delta\phi) \\ &+ T^A_3 T^B_2 \cos(\varepsilon_k t + \theta - \Delta\phi) + T^B_3 T^A_2 \cos(\varepsilon_k t - \theta + \Delta\phi)\big], \end{aligned} \tag{A6}$$

where $T^{A/B}_2$ and $T^{A/B}_3$ are two-photon and three-photon transition matrix elements. Of note is that the transition probabilities do not depend on the angular distribution of the initial electronic state, i.e., $T^{A/B}_{2/3}$ is θ independent.

Assuming the same transition matrix elements of the multiphoton ionization, i.e., $T = T^{A/B}_{2/3}$, Eq. (A6) then can be rewritten as

$$P^I_{\rm int}(\varepsilon_k, \theta, \Delta\phi, t) = 2E^4_\omega E_{2\omega} f^5(t) T[\cos(\theta - \Delta\phi) + \cos(\varepsilon_k t)\cos(\theta - \Delta\phi)]. \tag{A7}$$

By integrating over time t with a Gaussian envelope $f(t) = e^{-\beta t^2/\tau}$, where τ is the FWHM (full width at half maximum), the interference term can be expressed as

$$P^I_{\rm int}(\varepsilon_k, \theta, \Delta\phi) = \alpha_{32}(\varepsilon_k)\cos(\theta - \Delta\phi), \tag{A8}$$

where

$$\alpha_{32}(\varepsilon_k) = \alpha_0 + \alpha_1 e^{-\alpha_2 \varepsilon_k^2}. \tag{A9}$$

The coefficients are given by

$$\alpha_0 = 2E_\omega^4 E_{2\omega} T \int_{-\infty}^{\infty} e^{-5\beta t^2/\tau}\, dt = 2E_\omega^4 E_{2\omega} T \sqrt{\pi/5\beta},$$

$$\alpha_1 = 2E_\omega^4 E_{2\omega} T \sqrt{\pi\tau/5\beta},$$

and

$$\alpha_2 = 1/20\beta.$$

These coefficients are determined by the laser pulses, i.e., the pulse intensity $E_{\omega/2\omega}$ and duration τ. As shown in Eq. (A8), the simple dependence on the pulse relative phase $\Delta\phi$ and photoelectron energy ε_k occurs in the multiple way interference for $3\omega_1$ and $\omega_1 + \omega_2$ ionization processes. The interference pattern is sensitive to the photoelectron angle, which is determined by the molecular orbital symmetry. Therefore, the dependence occurs by averaging over molecular orientations.

For the second ATI peak, the molecule is ionized from the $A\,^2\Sigma^+$ and $B\,^2\Pi$ states via three pathways, four ω_1, three $\omega_1 + \omega_1 + \omega_2$, and two $\omega_2 + \omega_2$ photons. The four ω_1 photon transition process is given by

$$P_{A/B}^{4\omega_1}(\varepsilon_k, t) = \frac{\langle\psi_i(\varepsilon_k)|\mu_{A/B}E_\omega(t)|\psi_3\rangle\langle\psi_3|\mu_{A/B}E_\omega(t)|\psi_2\rangle\langle\psi_2|\mu_{A/B}E_\omega(t)|\psi_1\rangle\langle\psi_1|\mu_{A/B}E_\omega(t)|\psi_{A/B}\rangle}{(E_{A/B} - E_3 + 3\omega)(E_{A/B} - E_2 + 2\omega)(E_{A/B} - E_1 + \omega)}. \tag{A10}$$

The three $2\omega_1 + \omega_2$ ionization is composed of three possible channels which read as

$$\begin{aligned} P_{A/B}^{2\omega_1+\omega_2}(\varepsilon_k, t) = {} & \frac{\langle\psi_i(\varepsilon_k)|\mu_{A/B}E_{2\omega}(t)|\psi_2\rangle\langle\psi_2|\mu_{A/B}E_\omega(t)|\psi_1\rangle\langle\psi_1|\mu_{A/B}E_\omega(t)|\psi_{A/B}\rangle}{(E_{A/B} - E_2 + 2\omega)(E_{A/B} - E_1 + \omega)} \\ & + \frac{\langle\psi_i(\varepsilon_k)|\mu_{A/B}E_\omega(t)|\psi_2\rangle\langle\psi_2|\mu_{A/B}E_{2\omega}(t)|\psi_1\rangle\langle\psi_1|\mu_{A/B}E_\omega(t)|\psi_{A/B}\rangle}{(E_{A/B} - E_3 + 3\omega)(E_{A/B} - E_1 + \omega)} \\ & + \frac{\langle\psi_i(\varepsilon_k)|\mu_{A/B}E_\omega(t)|\psi_2\rangle\langle\psi_2|\mu_{A/B}E_\omega(t)|\psi_1\rangle\langle\psi_1|\mu_{A/B}E_{2\omega}(t)|\psi_{A/B}\rangle}{(E_{A/B} - E_3 + 3\omega)(E_{A/B} - E_2 + 2\omega)}. \end{aligned} \tag{A11}$$

And the two ω_2 photon process is

$$P_{A/B}^{2\omega_2}(\varepsilon_k, t) = \frac{\langle\psi_i(\varepsilon_k)|\mu_{A/B}E_{2\omega}(t)|\psi_1\rangle\langle\psi_1|\mu_{A/B}E_{2\omega}(t)|\psi_{A/B}\rangle}{E_{A/B} - E_2 + 2\omega}. \tag{A12}$$

These multiphoton ionization processes interfere with each other. We then obtain

$$P_{\rm int}^{II1}(\varepsilon_k, t) = \left[P_A^{4\omega_1}(\varepsilon_k, t) + P_B^{4\omega_1}(\varepsilon_k, t)\right]^* \left[P_A^{2\omega_1+\omega_2}(\varepsilon_k, t) + P_B^{2\omega_1+\omega_2}(\varepsilon_k, t)\right] + \text{c.c.} \tag{A13}$$

for the four-photon $P_{A/B}^{4\omega_1}(\varepsilon_k, t)$ and three-photon $P_{A/B}^{2\omega_1+\omega_2}(\varepsilon_k, t)$ interference and

$$P_{\rm int}^{II2}(\varepsilon_k, t) = \left[P_A^{2\omega_2}(\varepsilon_k, t) + P_B^{2\omega_2}(\varepsilon_k, t)\right]^* \left[P_A^{2\omega_1+\omega_2}(\varepsilon_k, t) + P_B^{2\omega_1+\omega_2}(\varepsilon_k, t)\right] + \text{c.c.} \tag{A14}$$

for the two-photon $P_{A/B}^{2\omega_2}(\varepsilon_k, t)$ and three-photon $P_{A/B}^{2\omega_1+\omega_2}(\varepsilon_k, t)$ interference. For both $P_{\rm int}^{II1}(\varepsilon_k, t)$ and $P_{\rm int}^{II2}(\varepsilon_k, t)$, the interference terms contain $\sim\cos(\theta - \Delta\phi)$. The four-photon $P_{A/B}^{4\omega_1}(\varepsilon_k, t)$ and two-photon $P_{A/B}^{2\omega_2}(\varepsilon_k, t)$ interference is expressed as

$$P_{\rm int}^{II3}(\varepsilon_k, t) = \left[P_A^{4\omega_1}(\varepsilon_k, t) + P_B^{4\omega_1}(\varepsilon_k, t)\right]^* \left[P_A^{2\omega_2}(\varepsilon_k, t) + P_B^{2\omega_2}(\varepsilon_k, t)\right] + \text{c.c.}, \tag{A15}$$

which is a function of $\cos^2(\theta - \Delta\phi)$.

For this multiple pathway ionization, the interference term is simply the sum of the contributions from all channels, i.e., $P_{\rm int}^{II}(\varepsilon_k) = P_{\rm int}^{II1}(\varepsilon_k) + P_{\rm int}^{II2}(\varepsilon_k) + P_{\rm int}^{II3}(\varepsilon_k)$. The interference term then can be given by

$$P_{\rm int}^{II}(\varepsilon_k, \theta, \Delta\phi) = [\alpha_{43}(\varepsilon_k) + \alpha_{32}(\varepsilon_k)]\cos(\theta - \Delta\phi) + \alpha_{42}(\varepsilon_k)\cos^2(\theta - \Delta\phi). \tag{A16}$$

The coefficients $\alpha_{ij}(\varepsilon_k)$ for the i and j photon ionizations are obtained by integrating over time t with a Gaussian envelope pulse.

The results for the photoelectron distribution of the third ATI peak arise from three pathway transitions after direct absorptions of five ω_1 photons, three ω_1 and one ω_2 photons, and one ω_1 and two ω_2 photons. The transition from the $A\,^2\Sigma^+$ and $B\,^2\Pi$ states is given by

$$P_{A/B}^{5\omega_1}(\varepsilon_k, t) = \frac{\langle\psi_i(\varepsilon_k)|\mu_{A/B}E_\omega(t)|\psi_4\rangle\langle\psi_4|\mu_{A/B}E_\omega(t)|\psi_3\rangle \ldots \langle\psi_2|\mu_{A/B}E_\omega(t)|\psi_1\rangle\langle\psi_1|\mu_{A/B}E_\omega(t)|\psi_{A/B}\rangle}{(E_{A/B} - E_4 + 4\omega)(E_{A/B} - E_3 + 3\omega)(E_{A/B} - E_2 + 2\omega)(E_{A/B} - E_1 + \omega)} \tag{A17}$$

for the five-photon ω_1 transition process,

$$P_{A/B}^{3\omega_1+\omega_2}(\varepsilon_k,t) = \frac{\langle\psi_i(\varepsilon_k)|\mu_{A/B}E_{2\omega}(t)|\psi_3\rangle\langle\psi_3|\mu_{A/B}E_{\omega}(t)|\psi_2\rangle\langle\psi_2|\mu_{A/B}E_{\omega}(t)|\psi_1\rangle\langle\psi_1|\mu_{A/B}E_{\omega}(t)|\psi_{A/B}\rangle}{(E_{A/B}-E_3+3\omega)(E_{A/B}-E_2+2\omega)(E_{A/B}-E_1+\omega)}$$
$$+\frac{\langle\psi_i(\varepsilon_k)|\mu_{A/B}E_{\omega}(t)|\psi_4\rangle\langle\psi_4|\mu_{A/B}E_{2\omega}(t)|\psi_2\rangle\langle\psi_2|\mu_{A/B}E_{\omega}(t)|\psi_1\rangle\langle\psi_1|\mu_{A/B}E_{\omega}(t)|\psi_{A/B}\rangle}{(E_{A/B}-E_4+4\omega)(E_{A/B}-E_2+2\omega)(E_{A/B}-E_1+\omega)}$$
$$+\frac{\langle\psi_i(\varepsilon_k)|\mu_{A/B}E_{\omega}(t)|\psi_4\rangle\langle\psi_4|\mu_{A/B}E_{\omega}(t)|\psi_3\rangle\langle\psi_3|\mu_{A/B}E_{2\omega}(t)|\psi_1\rangle\langle\psi_1|\mu_{A/B}E_{\omega}(t)|\psi_{A/B}\rangle}{(E_{A/B}-E_4+4\omega)(E_{A/B}-E_3+3\omega)(E_{A/B}-E_1+\omega)}$$
$$+\frac{\langle\psi_i(\varepsilon_k)|\mu_{A/B}E_{\omega}(t)|\psi_4\rangle\langle\psi_4|\mu_{A/B}E_{\omega}(t)|\psi_3\rangle\langle\psi_3|\mu_{A/B}E_{\omega}(t)|\psi_2\rangle\langle\psi_2|\mu_{A/B}E_{2\omega}(t)|\psi_{A/B}\rangle}{(E_{A/B}-E_4+4\omega)(E_{A/B}-E_3+3\omega)(E_{A/B}-E_2+2\omega)} \tag{A18}$$

for the four-photon $3\omega_1+\omega_2$ ionization, and

$$P_{A/B}^{\omega_1+2\omega_2}(\varepsilon_k,t) = \frac{\langle\psi_i(\varepsilon_k)|\mu_{A/B}E_{2\omega}(t)|\psi_3\rangle\langle\psi_3|\mu_{A/B}E_{2\omega}(t)|\psi_1\rangle\langle\psi_1|\mu_{A/B}E_{\omega}(t)|\psi_{A/B}\rangle}{(E_{A/B}-E_3+3\omega)(E_{A/B}-E_1+\omega)}$$
$$+\frac{\langle\psi_i(\varepsilon_k)|\mu_{A/B}E_{2\omega}(t)|\psi_3\rangle\langle\psi_3|\mu_{A/B}E_{\omega}(t)|\psi_2\rangle\langle\psi_2|\mu_{A/B}E_{2\omega}(t)|\psi_{A/B}\rangle}{(E_{A/B}-E_3+3\omega)(E_{A/B}-E_2+2\omega)}$$
$$+\frac{\langle\psi_i(\varepsilon_k)|\mu_{A/B}E_{\omega}(t)|\psi_4\rangle\langle\psi_4|\mu_{A/B}E_{2\omega}(t)|\psi_2\rangle\langle\psi_2|\mu_{A/B}E_{2\omega}(t)|\psi_{A/B}\rangle}{(E_{A/B}-E_4+4\omega)(E_{A/B}-E_2+2\omega)} \tag{A19}$$

for the three-photon $\omega_1+2\omega_2$ process. Similarly, the interference term gives $P_{\rm int}^{III}(\varepsilon_k) = P_{\rm int}^{III1}(\varepsilon_k) + P_{\rm int}^{III2}(\varepsilon_k) + P_{\rm int}^{III3}(\varepsilon_k)$, where

$$P_{\rm int}^{III1}(\varepsilon_k,t) = \left[P_A^{5\omega_1}(\varepsilon_k,t) + P_B^{5\omega_1}(\varepsilon_k,t)\right]^*\left[P_A^{3\omega_1+\omega_2}(\varepsilon_k,t) + P_B^{3\omega_1+\omega_2}(\varepsilon_k,t)\right] + \text{c.c.} \tag{A20}$$

for the five-photon $P_{A/B}^{5\omega_1}(\varepsilon_k,t)$ and four-photon $P_{A/B}^{3\omega_1+\omega_2}(\varepsilon_k,t)$ interference,

$$P_{\rm int}^{III2}(\varepsilon_k,t) = \left[P_A^{3\omega_1+\omega_2}(\varepsilon_k,t) + P_B^{3\omega_1+\omega_2}(\varepsilon_k,t)\right]^*\left[P_A^{\omega_1+2\omega_2}(\varepsilon_k,t) + P_B^{\omega_1+2\omega_2}(\varepsilon_k,t)\right] + \text{c.c.} \tag{A21}$$

for the four-photon $P_{A/B}^{3\omega_1+\omega_2}(\varepsilon_k,t)$ and three-photon $P_{A/B}^{\omega_1+2\omega_2}(\varepsilon_k,t)$ interference, and

$$P_{\rm int}^{III3}(\varepsilon_k,t) = \left[P_A^{5\omega_1}(\varepsilon_k,t) + P_B^{5\omega_1}(\varepsilon_k,t)\right]^*\left[P_A^{\omega_1+2\omega_2}(\varepsilon_k,t) + P_B^{\omega_1+2\omega_2}(\varepsilon_k,t)\right] + \text{c.c.} \tag{A22}$$

for the five-photon $P_{A/B}^{5\omega_1}(\varepsilon_k,t)$ and three-photon $P_{A/B}^{\omega_1+2\omega_2}(\varepsilon_k,t)$ interference, where $P_{\rm int}^{III1}(\varepsilon_k,t)$ and $P_{\rm int}^{III2}(\varepsilon_k,t)$ are a function of $\cos(\theta-\Delta\phi)$ and $P_{\rm int}^{III3}(\varepsilon_k,t) \sim \cos^2(\theta-\Delta\phi)$. As a result, the three-pathway ionization interference term of the third ATI peak can be written as, by integrating over time t,

$$P_{\rm int}^{III}(\varepsilon_k,\theta,\Delta\phi) = [\alpha_{54}(\varepsilon_k)+\alpha_{43}(\varepsilon_k)]\cos(\theta-\Delta\phi) + \alpha_{53}(\varepsilon_k)\cos^2(\theta-\Delta\phi). \tag{A23}$$

From Eqs. (A16) and (A23) one sees that the second and the third ATI photoelectron distributions have the similar interference forms. Both odd and even powers of $\cos(\theta-\Delta\phi)$ are obtained in the interference terms, that is, an even number of transition $\cos^2(\theta-\Delta\phi)$ terms occur for odd-odd or even-even parity interferences, whereas the term $\cos(\theta-\Delta\phi)$ corresponds to odd-even transition interferences.

[1] J. Manz and L. Wöste, *Femtosecond Chemistry* (VCH Verlagsgesellschaft mbH, Weinheim, 1995).
[2] A. H. Zewail, J. Phys. Chem. A **104**, 5660 (2000).
[3] T. Wang, T. Yang, C. Xiao, Z. Sun, D. Zhang, X. Yang, M. L. Weichman, and D. M. Neumark, Chem. Soc. Rev. **47**, 6744 (2018).
[4] A. D. Bandrauk, *Molecules in Laser Fields* (Marcel Dekker, New York, 1994).
[5] P. H. Bucksbaum, A. Zavriyev, H. G. Muller, and D. W. Schumacher, Phys. Rev. Lett. **64**, 1883 (1990).
[6] L. J. Frasinski, J. H. Posthumus, J. Plumridge, K. Codling, P. F. Taday, and A. J. Langley, Phys. Rev. Lett. **83**, 3625 (1999).
[7] G. Yao and S.-I. Chu, Phys. Rev. A **48**, 485 (1993).
[8] G. Jolicard and O. Atabek, Phys. Rev. A **46**, 5845 (1992).
[9] A. Giusti-Suzor, X. He, O. Atabek, and F. H. Mies, Phys. Rev. Lett. **64**, 515 (1990).
[10] S. Luo, S. Zhou, W. Hu, X. Li, P. Ma, J. Yu, R. Zhu, C. Wang, F. Liu, B. Yan, A. Liu, Y. Yang, F. Guo, and D. Ding, Phys. Rev. A **96**, 063415 (2017).
[11] A. McPherson, G. Gibson, H. Jara, U. Johann, T. S. Luk, I. A. McIntyre, K. Boyer, and C. K. Rhodes, J. Opt. Soc. Am. B **4**, 595 (1987).
[12] M. Ferray, A. L'Huillier, X. F. Li, L. A. Lompre, G. Mainfray, and C. Manus, J. Phys. B: At., Mol. Opt. Phys. **21**, L31 (1988).
[13] K. Wilma, C. Shu, U. Scherf, and R. Hildner, J. Am. Chem. Soc. **140**, 15329 (2018).
[14] K. Wilma, C.-C. Shu, U. Scherf, and R. Hildner, New J. Phys. **21**, 045001 (2019).
[15] G. J. Halász, Á. Vibók, and L. S. Cederbaum, J. Phys. Chem. Lett. **6**, 348 (2015).
[16] C. C. Shu, K. J. Yuan, D. Dong, I. R. Petersen, and A. D. Bandrauk, J. Phys. Chem. Lett. **8**, 1 (2017).

[17] A. Tóth, A. Csehi, G. J. Halász, and Á. Vibók, Phys. Rev. A **99**, 043424 (2019).

[18] Y. Nabekawa, Y. Furukawa, T. Okino, A. A. Eilanlou, E. J. Takahashi, K. Yamanouchi, and K. Midorikawa, Sci. Rep. **5**, 11366 (2015).

[19] Y. Nabekawa, Y. Furukawa, T. Okino, A. A. Eilanlou, E. J. Takahashi, K. Yamanouchi, and K. Midorikawa, Nat. Commun. **6**, 8197 (2015).

[20] K. J. Schafer, B. Yang, L. F. DiMauro, and K. C. Kulander, Phys. Rev. Lett. **70**, 1599 (1993).

[21] W. Becker, F. Grasbon, R. Kopold, D. B. Milosevic, G. G. Paulus, and H. Walther, Adv. Atom. Mol. Opt. Phys. **48**, 35 (2002).

[22] N. Suárez, A. Chacón, M. F. Ciappina, B. Wolter, J. Biegert, and M. Lewenstein, Phys. Rev. A **94**, 043423 (2016).

[23] C. Wang, M. Okunishi, X. Hao, Y. Ito, J. Chen, Y. Yang, R. R. Lucchese, M. Zhang, B. Yan, W. D. Li, D. Ding, and K. Ueda, Phys. Rev. A **93**, 043422 (2016).

[24] H. Liang, X.-R. Xiao, Q. Gong, and L.-Y. Peng, J. Phys. B: At., Mol. Opt. Phys. **50**, 174002 (2017).

[25] T. Zuo, A. D. Bandrauk, and P. B. Corkum, Chem. Phys. Lett. **259**, 313 (1996).

[26] M. Meckel, D. Comtois, D. Zeidler, A. Staudte, D. Pavicic, H. C. Bandulet, H. Pepin, J. C. Kieffer, R. Dörner, D. M. Villeneuve, and P. B. Corkum, Science **320**, 1478 (2008).

[27] M. Peters, T. T. Nguyen-Dang, E. Charron, A. Keller, and O. Atabek, Phys. Rev. A **85**, 053417 (2012).

[28] Y. Huismans *et al.*, Science **331**, 61 (2011).

[29] X. B. Bian, Y. Huismans, O. Smirnova, K. J. Yuan, M. J. J. Vrakking, and A. D. Bandrauk, Phys. Rev. A **84**, 043420 (2011).

[30] M. Okunishi, R. Itaya, K. Shimada, G. Prümper, K. Ueda, M. Busuladžić, A. Gazibegović-Busuladžić, D. B. Milošević, and W. Becker, Phys. Rev. Lett. **103**, 043001 (2009).

[31] M. Li, W.-C. Jiang, H. Xie, S. Luo, Y. Zhou, and P. Lu, Phys. Rev. A **97**, 023415 (2018).

[32] K. L. Reid, D. J. Leahy, and R. N. Zare, J. Chem. Phys. **95**, 1746 (1991).

[33] A. Sen, S. T. Pratt, and K. L. Reid, J. Chem. Phys. **147**, 013927 (2017).

[34] M. G. White, M. Seaver, W. A. Chupka, and S. D. Colson, Phys. Rev. Lett. **49**, 28 (1982).

[35] H. Rudolph and V. McKoy, J. Chem. Phys. **91**, 2235 (1989).

[36] J. B. M. Warntjes, F. Robicheaux, J. M. Bakker, and L. D. Norrdam, J. Chem. Phys. **111**, 2556 (1999).

[37] P. Ludowise, M. Blackwell, and Y. Chen, Chem. Phys. Lett. **258**, 530 (1996).

[38] Z. G. Sun, S. L. Cong, N. Q. Lou, and K. L, Han, Chem. Phys. Chem. **3**, 976 (2002).

[39] Z. G. Sun, H. P. Liu, N. Q. Lou, and S. L. Cong, Chem. Phys. Lett. **369**, 374 (2003).

[40] S. M. Wang, S. L. Cong, K. J. Yuan, and Y. Y. Niu, Chem. Phys. Lett. **417**, 164 (2006).

[41] Q. T. Meng, G. H. Yang, H. L. Sun, K. L. Han, and N. Q. Lou, Phys. Rev. A **67**, 063202 (2003).

[42] B. X. Wang, B. K. Liu, Y. Q. Wang, and L. Wang, Phys. Rev. A **81**, 043421 (2010).

[43] O. Faucher, E. Hertz, B. Lavorel, R. Chaux, T. Dreier, H. Berger, and D. Charalambidis, J. Phys. B **32**, 4485 (1999).

[44] R. B. López-Martens, T. W. Schmidt, and G. Roberts, Phys. Rev. A **62**, 013414 (2000).

[45] T. W. Schmidt, R. B. López-Martens, and G. Roberts, J. Phys. B: At., Mol. Opt. Phys. **37**, 1125 (2004).

[46] A. Gijsbertsen, W. Siu, M. F. Kling, P. Johnsson, P. Jansen, S. Stolte, and M. J. J. Vrakking, Phys. Rev. Lett. **99**, 213003 (2007).

[47] S. Chelkowski, T. Bredtmann, and A. D. Bandrauk, Phys. Rev. A **85**, 033404 (2012).

[48] T. Bredtmann, S. Chelkowski, and A. D. Bandrauk, J. Phys. Chem A **116**, 11398 (2012).

[49] G. Goldsztejn, T. Marchenko, D. Céolin, L. Journel, R. Guillemin, J.-P. Rueff, R. K. Kushawaha, R. Püttner, M. N. Piancastelli, and M. Simon, Phys. Chem. Chem. Phys. **18**, 15133 (2016).

[50] S. Nandi, C. Nicolas, A. N. Artemyev, N. M. Novikovskiy, C. Miron, J. D. Bozek, and Ph. V. Demekhin, Phys. Rev. A **96**, 052501 (2017).

[51] W. Hu, Y. Liu, S. Luo, X. Li, J. Yu, X. Li, Z. Sun, K. J. Yuan, A. D. Bandrauk, and D. Ding, Phys. Rev. A **99**, 011402(R) (2019).

[52] K. Ueda, C. Miron, E. Plésiat, L. Argenti, M. Patanen, K. Kooser, D. Ayuso, S. Mondal, M. Kimura, K. Sakai, O. Travnikova, A. Palacios, P. Decleva, E. Kukk, and F. Martín, J. Chem. Phys. **139**, 124306 (2013)

[53] D. Ayuso, M. Kimura, K. Kooser, M. Patanen, E. Plésiat, L. Argenti, S. Mondal, O. Travnikova, K. Sakai, A. Palacios, E. Kukk, P. Decleva, K. Ueda, F. Martín, and C. Miron, J. Phys. Chem. A **119**, 5971 (2015).

[54] R. Y. Bello, S. E. Canton, D. Jelovina, J. D. Bozek, B. Rude, O. Smirnova, M. Y. Ivanov, A. Palacios, and F. Martín, Sci. Adv. **4**, eaat3962 (2018).

[55] G. Hermann, C. Liu, J. Manz, B. Paulus, J. F. Pérez-Torres, V. Pohl, and J. C. Tremblay, J. Phys. Chem. A **120**, 5360 (2016).

[56] D. Jia, J. Manz, B. Paulus, V. Pohl, J. C. Tremblay, and Y. Yang, Chem. Phys. **482**, 146 (2017).

[57] H. J. Wörner, J. B. Bertrand, P. Hockett, P. B. Corkum, and D. M. Villeneuve, Phys. Rev. Lett. **104**, 233904 (2010).

[58] A. Rupenyan, P. M. Kraus, J. Schneider, and H. J. Wörner, Phys. Rev. A **87**, 031401(R) (2013).

[59] A. Leclerc, D. Viennot, G. Jolicard, R. Lefebvre, and O. Atabek, J. Phys. B: At., Mol. Opt. Phys. **50**, 234002 (2017).

[60] P. M. Kraus, B. Mignolet, D. Baykusheva, A. Rupenyan, L. Horný, E. F. Penka, G. Grassi, O. I. Tolstikhin, J. Schneider, F. Jensen, L. B. Madsen, A. D. Bandrauk, F. Remacle, and H. J. Wörner, Science **350**, 790 (2015).

[61] A. T. J. B. Eppink, and D. H. Parker, Rev. Sci. Instrum. **68**, 3477 (1997).

[62] M. J. J. Vrakking, Rev. Sci. Instrum. **72**, 4084 (2001).

[63] Y. Shao, M. Li, M.-M. Liu, X. Sun, X. Xie, P. Wang, Y. Deng, C. Wu, Q. Gong, and Y. Liu, Phys. Rev. A **92**, 013415 (2015).

[64] O. Hüter and F. Temps, Rev. Sci. Instrum. **88**, 046101 (2017).

[65] F. R. Gillmorre, J. Quant. Spectrosc. Radiat. Transfer. **5**, 369 (1965).

[66] C. Meier and V. Engel, Phys. Rev. Lett. **73**, 3207 (1994).

[67] Z. Sun and N. Lou, Phys. Rev. Lett. **91**, 023002 (2003).

[68] J. T. Muckerman, Chem. Phys. Lett. **73**, 200 (1990).

[69] D. T. Colbert and W. H. Miller, J. Chem. Phys. **96**, 1982 (1992).
[70] M. D. Feit and J. A. Fleck, Jr., J. Chem. Phys. **78**, 301 (1982); M. D. Feit and J. A. Fleck Jr., J. Comput. Phys. **47**, 412 (1983).
[71] A. D. Bandrauk and H. Shen, J. Chem. Phys. **99**, 1185 (1993); A. D. Bandrauk and H. Lu, J. Theor. Comput. Chem. **12**, 1340001 (2013).
[72] J. Wu, L. Ph. H. Schmidt, M. Kunitski, M. Meckel, S. Voss, H. Sann, H. Kim, T. Jahnke, A. Czasch, and R. Dörner, Phys. Rev. Lett. **108**, 183001 (2012).
[73] T. Endo, A. Matsuda, M. Fushitani, T. Yasuike, O. I. Tolstikhin, T. Morishita, and A. Hishikawa, Phys. Rev. Lett. **116**, 163002 (2016).
[74] G. Lagmago Kamta and A. D. Bandrauk, Phys. Rev. A **74**, 033415 (2006).
[75] A. L'Huillier, L. A. Lompré, D. Normand, X. Tang, and P. Lambropoulos, J. Opt. Soc. Am. B **6**, 1790 (1989).
[76] F. Fillion-Gourdeau, E. Lorin, and A. D. Bandrauk, J. Phys. A: Math. Theor. **45**, 215304 (2012).
[77] H. L. Kim and R. Bersohn, J. Chem. Phys. **107**, 4546 (1997).
[78] J. M. Ngoko Djiokap, S. X. Hu, L. B. Madsen, N. L. Manakov, A. V. Meremianin, and A. F. Starace, Phys. Rev. Lett. **115**, 113004 (2015).
[79] K. J. Yuan, S. Chelkowski, and A. D. Bandrauk, Phys. Rev. A **93**, 053425 (2016).
[80] L. J. Zipp, A. Natan, and P. H. Bucksbaum, Optica **1**, 361 (2014).
[81] X. Gong, C. Lin, F. He, Q. Song, K. Lin, Q. Ji, W. Zhang, J. Ma, P. Lu, Y. Liu, H. Zeng, W. Yang, and J. Wu, Phys. Rev. Lett. **118**, 143203 (2017).
[82] X. Song, G. Shi, G. Zhang, J. Xu, C. Lin, J. Chen, and W. Yang, Phys. Rev. Lett. **121**, 103201 (2018).
[83] J. Li, X. Ren, Y. Yin, K. Zhao, A. Chew, Y. Cheng, E. Cunningham, Y. Wang, S. Hu, Y. Wu, M. Chini, and Z. Chang, Nat. Commun. **8**, 186 (2017).
[84] T. Gaumnitz, A. Jain, Y. Pertot, M. Huppert, I. Jordan, F. Ardana-Lamas, and H. J. Wörner, Opt. Express **25**, 27506 (2017).
[85] K. J. Yuan, C. C. Shu, D. Dong, and A. D. Bandrauk, J. Phys. Chem. Lett. **8**, 2229 (2017).
[86] M. Lara-Astiaso, M. Galli, A. Trabattoni, A. Trabattoni, A. Palacios, D. Ayuso, F. Frassetto, L. Poletto, S. De Camillis, J. Greenwood, P. Decleva, I. Tavernelli, F. Calegari, M. Nisoli, and F. Martín, J. Phys. Chem. Lett. **9**, 4570 (2018).
[87] F. H. M. Faisal, *Theory of Multiphoton Processes* (Springer, New York, 1987).